RANSAC-Based Fault Detection and Exclusion Algorithm for Single-Difference Tightly Coupled GNSS/INS Integration

Quan Zhang, *Member, IEEE*, Huan Lin, Longyang Ding, Qijin Chen, Tisheng Zhang, and Xiaoji Niu

***Abstract*—There is an urgent need for high-accuracy and high-reliability navigation and positioning in life safety fields such as intelligent transportation and automotive driving, especially in complex urban environments. Although, compared with the GNSS and loosely coupled integration, a tightly coupled GNSS/INS integration can improve the positioning reliability by using raw observations, it still suffers from external challenging environments such as the multipath effect. Therefore, the fault detection algorithm is a premise and guarantee to realize quality control of GNSS/INS integration. Inspired by the application of the random sample consensus (RANSAC) algorithm in GNSS fault detection, this article proposes a RANSAC-based fault detection and exclusion algorithm for single-difference tightly coupled GNSS/INS integration. Here, a between-receiver single-difference (BRSD) model was designed to prevent the consumption of GNSS observations and reduce the waste of effective parameters, and the global proportion statistics of faults were introduced into the typical RANSAC algorithm to further ensure detection reliability. In this study, the effect of the main parameters on the proposed detection algorithm was analyzed and verified by artificial cycle slips. Multiple filed tests, including typical urban scenarios, were conducted to verify the feasibility and effectiveness of the proposed method. The comprehensive test results show that the north and east positioning accuracy in terms of cumulative distribution function (CDF, CDF = 95%) are improved by 45% and 42% over the tightly coupled mode without the proposed detection method.**

***Index Terms*—Fault detection, RANSAC, tightly coupled, between-receiver single difference, GNSS/INS integration.**

Manuscript received 24 October 2023; revised 24 November 2023; accepted 9 December 2023. This work was supported in part by the National Key Research and Development Program of China under Grant 2022YFB3903802, in part by the National Natural Science Foundation of China under Grant 42174024, and in part by AGRS Youth Innovation Foundation under Grant 2020YFL07. *(Quan Zhang and Huan Lin are co-first authors.) (Corresponding authors: Xiaoji Niu; Qijin Chen.)*

Quan Zhang, Qijin Chen, and Tisheng Zhang are with GNSS Research Center, Wuhan University, Wuhan 430072, China, and also with Hubei Luojia Laboratory, Wuhan 430072, China (e-mail: zhangquan@whu.edu.cn; chenqijin@whu.edu.cn; zts@whu.edu.cn).

Huan Lin and Longyang Ding are with GNSS Research Center, Wuhan University, Wuhan 430072, China (e-mail: 2015301610082@whu.edu.cn; dingly@whu.edu.cn).

Xiaoji Niu is with GNSS Research Center, Wuhan University, Wuhan 430072, China, also with Hubei Luojia Laboratory, Wuhan 430072, China, and also with the Artificial Intelligence Institute of Wuhan University, Wuhan 430072, China (e-mail: xjniu@whu.edu.cn).

Color versions of one or more figures in this article are available at https://doi.org/10.1109/TIV.2023.3342274.

Digital Object Identifier 10.1109/TIV.2023.3342274

I. Introduction

The integration of the global navigation satellite system (GNSS) with an inertial navigation system (INS) can achieve complementary advantages, providing pose services with high accuracy and continuity for the intelligent vehicle navigation and control. There has been an increasing demand for the positioning accuracy and reliability of GNSS/INS integration, especially using low-cost sensors (e.g., microelectromechanical system (MEMS) inertial measurement unit (IMU)), in safety of life applications such as intelligent driving [1], [2]. However, complex urban environments bring severe challenges to GNSS observation. For example, satellite visibility is completely or partially obscured in urban environments, which results in a decrease in GNSS positioning accuracy and continuity [3], [4].

Tightly coupled (TC) GNSS/INS integration can directly utilize raw GNSS observations for measurement updates and performs better than loosely coupled (LC) integration in areas with partially blocked GNSS access [5]. Although GNSS/INS integration can ensure positioning continuity, satellite signals are still interfered by the non-line-of-sight (NLOS) signals and multipath effects, resulting in GNSS observation faults and ultimately affecting the positioning accuracy and reliability in challenging environments. Therefore, quality control is a prerequisite to correctly detect faults and improve positioning accuracy and reliability. Common GNSS/INS integration fault detection methods are conducted by constructing test statistics based on the innovation vector of a Kalman filter [6], [7]. These methods apply quality control at the information fusion level and are not effective for multiple faults detection. Classical receiver autonomous integrity monitoring (RAIM) algorithms have been developed to provide fault detection and exclusion (FDE) [8], [9], but they generally work properly in the case of a single fault and cannot provide reliable multiple faults detection capabilities. Although there are some methods such as multiple hypothesis solution separation (MHSS) and an advanced RAIM (ARAIM) method to solving multiple faults, these methods will be ineffective in presence of significantly large biases or large proportion of faulty satellites [10], [11].

Random sample consensus (RANSAC) can achieve correct GNSS fault detection in cases of multiple and small faults, and it is the research hotspot of GNSS fault detection and exclusion [12]. RANSAC is an iterative method to estimate the parameters of a mathematical model from a set of observed data that contains faults, and it can be interpreted as a fault detection method. The RANSAC algorithm was first proposed by Fischler and Bolles [13] and has been widely used in the field of computer vision and is capable of interpreting or smoothing data containing a significant percentage of faults [14]. Schroth et al. [15] first proposed the range consensus (RANCO) algorithm and the suggestion range consensus (S-RANCO) algorithm to detect faulty GNSS range measurements based on the elementary idea of the RANSAC algorithm. Furthermore, Schroth et al. [16] optimized the performance of RANCO by enhancing the subset evaluation, the subset selection algorithm and the modified threshold definition to significantly reduce the missed detection rate and false alarm rate.

On the basis of Schroth's research work, many performance (in terms of accuracy, effectiveness, and stability) improvement methods have been studied. Groves and Jiang et al. [17], [18] applied weighting based on consistency and C/N$_0$ to the common RANSAC cost function to reduce the number of the largest GNSS faults and used four GNSS measurements plus a height-aiding measurement instead of 5 GNSS measurements to improve the positioning accuracy. Su et al. [19] proposed a fast RANSAC algorithm using geometric dilution of precision (GDOP), the line-of-sight (LOS) vector and singular value decomposition (SVD) for subset preselection to solve the large computational load problem in the traditional RANSAC algorithm. An augmented version of the RANSAC algorithm that performs a final range comparison using the state estimate obtained with only the inliers identified by RANSAC was proposed for more reliable availability [20]. Zhao et al. [21] proposed a modified RANCO algorithm based on a genetic algorithm to inhibit the amount of exponential calculation. In addition, the RANSAC algorithm was introduced to protect the robustness and accuracy of a multi-GNSS time-difference carrier phase (TDCP) solution [22].

Currently, the RANSAC algorithm is applied to the fault detection and exclusion of individual GNSS range measurements, and the relevant research focuses on improving the computational efficiency and fault identification precision. Although some research has utilized the RANSAC algorithm to address the issue of loosely coupled GNSS/INS integration as demonstrated in some studies [23], [24], a critical unresolved problem pertains to the minimum number of satellites required in subset construction. This issue remains unsolved, and it is still necessary to use a minimum of four satellites. The existing relevant research does not design the RANSAC-based algorithm in the tightly coupled GNSS/INS integration, and not fully play the auxiliary role of inertial navigation information in the subset construction.

Inspired by its application to GNSS positioning solutions, RANSAC is applied to single-difference tightly coupled GNSS/INS integration for robust and high-accuracy positioning in this study. The characteristics and contribution of RANSAC-based fault detection in the context of single-difference tightly coupled GNSS/INS integrated navigation can be summarized as follows:

- A between-receiver single-difference (BRSD) tightly coupled GNSS/INS integration mode is designed. This mode reduces the effect of biases such as satellite-related error and atmospheric error, and allows for full utilization of more available GNSS observations.
- Based on the tightly coupled model, a RANSAC-based fault detection algorithm is presented. It can directly utilize two satellites as subset sample with the help of inertial navigation information. In addition, the global proportion statistics method is introduced into the typical RANSAC algorithm to further ensure detection reliability.

This article mainly presents the feasibility of RANSAC-based algorithm to detecting faults in tightly coupled GNSS/INS integration. The rest of this article is organized as follows. Section II illustrates single-difference tightly coupled GNSS/INS integration. Section III briefly introduces the principle of the RANSAC algorithm. Section IV expounds on the RANSAC-based fault detection and exclusion algorithm for single-difference tightly coupled GNSS/INS integration. In Section V, the effect of the main influencing factors on the proposed fault detection method is analyzed and validated. In Section VI, land vehicle tests, including typical scenarios, are conducted, and the experimental results are analyzed and discussed. Finally, the conclusion and characteristics of the proposed RANSAC-based fault detection and exclusion algorithm are summarized in Section VII.

II. Tightly Coupled GNSS/INS Integrated Navigation

An observation model of tightly coupled GNSS/INS integration can be constructed according to a GNSS positioning algorithm. Here, it is based on the between-receiver single-difference model to avoid the consumption of observation information and reduce the waste of effective parameters.

An augmented Kalman filter is applied to online estimate and compensate for sensor errors, including IMU error, single-difference GNSS clock error and ambiguity. Fig. 1 shows a block diagram of tightly coupled GNSS RTK/INS integration. Because tightly coupled GNSS/INS integration research is relatively mature, the design of the state model and observation model is only briefly described.

A. State Model

In GNSS/INS integration, the error state equations of the Kalman filter are commonly based on the error dynamic equations of the INS. The propagation of IMU errors in a given frame can be defined by a set of coupled differential equations based on the inertial navigation equations. Considering the IMU error, the INS error dynamic equations with respect to the navigation reference frame can be written as follows [25]:

$$
\begin{aligned}
\delta \dot{\boldsymbol{r}}^n &= F \cdot \delta \boldsymbol{r}^n + \delta \boldsymbol{v}^n \\
\delta \dot{\boldsymbol{v}}^n &= C_b^n \delta \boldsymbol{f}^b + C_b^n \boldsymbol{f}^b \times \phi - (2\boldsymbol{\omega}_{ie}^n + \boldsymbol{\omega}_{en}^n) \times \delta \boldsymbol{v}^n \\
&\quad + \boldsymbol{v}^n \times (2\delta\boldsymbol{\omega}_{ie}^n + \delta\boldsymbol{\omega}_{en}^n) + \delta \boldsymbol{g}^n \\
\dot{\phi} &= -\boldsymbol{\omega}_{in}^n \times \phi - C_b^n \delta \boldsymbol{\omega}_{ib}^b + \delta \boldsymbol{\omega}_{in}^n \\
\dot{\boldsymbol{b}}_g &= -\frac{1}{T}\boldsymbol{b}_g + \boldsymbol{w}_{bg} \\
\dot{\boldsymbol{b}}_a &= -\frac{1}{T}\boldsymbol{b}_a + \boldsymbol{w}_{ba}
\end{aligned}
$$

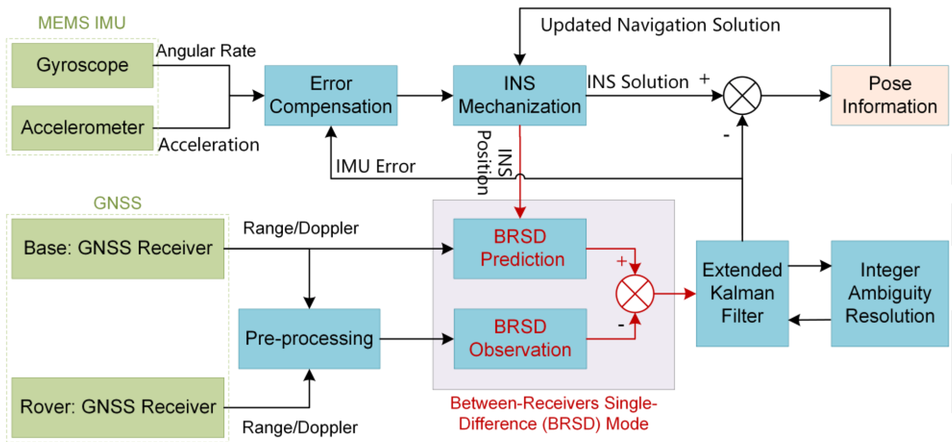

Fig. 1. Block diagram of tightly coupled GNSS RTK/INS integration based on a between-receiver single-difference model.

$$\begin{aligned}\dot{\boldsymbol{s}}_g &= -\frac{1}{T}\boldsymbol{s}_g + \boldsymbol{w}_{sg}\\ \dot{\boldsymbol{s}}_a &= -\frac{1}{T}\boldsymbol{s}_a + \boldsymbol{w}_{sa}\end{aligned} \tag{1}$$

where F is the coefficient matrix of the position error; $\delta \boldsymbol{r}^n$, $\delta \boldsymbol{v}^n$ and ϕ represent the position, velocity and attitude error in the navigation frame, respectively, and $\delta \dot{\boldsymbol{r}}^n$, $\delta \dot{\boldsymbol{v}}^n$ and $\dot{\phi}$ are the corresponding time derivative; $\boldsymbol{f}^b$ is the specific force outputted by the accelerometers; $\delta \boldsymbol{f}^b$ and $\delta \boldsymbol{\omega}_{ib}^b$ represent the sensor errors of the accelerometers and gyroscopes, including the bias ($\boldsymbol{b}_g$ and $\boldsymbol{b}_a$) and scale factor ($\boldsymbol{s}_g$ and $\boldsymbol{s}_a$) which are modeled as 1st Gauss-Markov process (where T is the correlation time and $\boldsymbol{w}$ is the driven white noise) and augmented to the error state vector for online estimation and compensation; C_b^n is the direction cosine matrix from the IMU frame to the navigation frame; $\boldsymbol{\omega}_{en}^n$, $\boldsymbol{\omega}_{ie}^n$ and $\boldsymbol{\omega}_{in}^n$ represent the angular rates of the navigation frame relative to the Earth frame, the Earth frame relative to the inertial frame and the navigation frame relative to the inertial frame in the navigation frame, respectively, and $\delta\boldsymbol{\omega}_{en}^n$, $\delta\boldsymbol{\omega}_{ie}^n$ and $\delta\boldsymbol{\omega}_{in}^n$ are the corresponding angular rate errors; $\delta \boldsymbol{g}^n$ is the normal gravity error at the local position; the superscripts n and b represent the navigation frame and the IMU frame, respectively; and $\times$ represents the cross product of vectors.

A between-receiver single-difference model can reduce the effect of satellite-related errors (e.g., clock error and orbit error) and spatial propagation errors (e.g., ionosphere error and troposphere error) with a baseline up to approximately 10 km [26]. Compared to a double-difference model, a between-receiver single-difference model needs to estimate the receiver clock error. In this article, the GNSS clock model consists of two parameters: clock error a_0 and clock drift a_1, and the drift is modeled as random walk. Hence, the GNSS clock model can be written as

$$\begin{aligned}\dot{a}_0 &= a_1 + w_0\\ \dot{a}_1 &= w_1\end{aligned} \tag{2}$$

where w_0 is the white noise of the clock error and w_1 is the driven white noise of the random walk.

The single-difference ambiguity ΔN is modeled as a random constant, and the corresponding model can be expressed as

$$\Delta \dot{N}_i = 0 \;\; (i = 1, \ldots, m) \tag{3}$$

where m represents the number of single-difference carrier phase observations and i is a visible satellite for the rover and base station in the same epoch.

The tightly coupled GNSS/INS integration state model based on the between-receiver single-difference model can be formed by combining (1), (2) and (3).

B. Observation Model

GNSS observations consist of the pseudorange, carrier phase and Doppler, and the corresponding between-receiver single-difference observation equations can be written as

$$\begin{aligned}\tilde{P}_{br}^s &= P_r^s - P_b^s = \rho_{br}^s + T_{bias}^{sys} + \varepsilon\\ \tilde{\varphi}_{br}^s &= \tilde{\varphi}_r^s - \tilde{\varphi}_b^s = \frac{1}{\lambda}\rho_{br}^s + \frac{1}{\lambda}T_{bias}^{sys} + \Delta N + \varepsilon\\ \tilde{D}_{br}^s &= -\frac{1}{\lambda}\left[\boldsymbol{e}_r^s\left(\boldsymbol{v}^s - \boldsymbol{v}_r\right) - \boldsymbol{e}_b^s\left(\boldsymbol{v}^s - \boldsymbol{v}_b\right)\right] + T_{drift} + \varepsilon\end{aligned} \tag{4}$$

where $\tilde{P}$, $\tilde{\varphi}$ and $\tilde{D}$ are the pseudorange, carrier phase and Doppler observations, respectively; the subscripts r and b represent the rover and base station, respectively; ρ_{br}^s is the single-difference range; T_{bias}^{sys} is the single-difference clock error, and it is the same as a_0 in (2); the superscript s represents a satellite; $T_{drift} = (df_r - df_b)$, and it is the single-difference clock drift that is the same as a_1 in (2); λ is the carrier wavelength; $\boldsymbol{e}_r^s$ and $\boldsymbol{e}_b^s$ are the LOS unit vectors between the rover/base station and the satellite, respectively; $\boldsymbol{v}^s$, $\boldsymbol{v}_r$ and $\boldsymbol{v}_b$ are the velocities of the satellite, rover and base station, respectively; and ε is the observation error.

Here, the expression of the observations derived from inertial navigation is directly given below. The derived range and Doppler observations based on the between-receiver single-difference model can be written as

$$\hat{\rho}_{br}^s = \rho_{br}^s - \boldsymbol{e}_r^s \delta \boldsymbol{r}^n - \boldsymbol{e}_r^s\left[\left(C_b^n \boldsymbol{l}_{GNSS}^b\right)\times\right]\phi$$

$$\hat{D}_{br}^{s} = -\frac{1}{\lambda}\left[\boldsymbol{e}_r^s\left(\boldsymbol{v}^s - \boldsymbol{v}_r^n\right) - \boldsymbol{e}_b^s\left(\boldsymbol{v}^s - \boldsymbol{v}_b^n\right)\right] + \frac{1}{\lambda}\boldsymbol{e}_r^s\delta\boldsymbol{v}^n \quad (5)$$

where $\boldsymbol{l}_{GNSS}^{b}$ represents the lever arm between the GNSS antenna and IMU center.

Combining (4) and (5) yields the observation equation of tightly coupled GNSS/INS integration based on the between-receiver single-difference model as follows:

$$\begin{aligned} z_P &= -\boldsymbol{e}_r^s\delta\boldsymbol{r}^n - \boldsymbol{e}_r^n\left[\left(C_b^n\boldsymbol{l}_{GNSS}^b\right)\times\right]\phi - T_{bias}^{sys} + \varepsilon \\ z_\phi &= -\frac{1}{\lambda}\boldsymbol{e}_r^s\delta\boldsymbol{r}^n - \frac{1}{\lambda}\boldsymbol{e}_r^s\left[\left(C_b^n\boldsymbol{l}_{GNSS}^b\right)\times\right]\phi \\ &\quad - \frac{1}{\lambda}T_{bias}^{sys} - \Delta N + \varepsilon \\ z_D &= \frac{1}{\lambda}\boldsymbol{e}_r^s\{\delta\boldsymbol{v}^n - \left[C_\omega\left(C_b^n\boldsymbol{l}_{GNSS}^b\times\right) + \left(C_l\boldsymbol{\omega}_{ib}^b\times\right)\right]\phi - C_l\boldsymbol{b}_g \\ &\quad - C_l diag\left(\boldsymbol{\omega}_{ib}^b\right)\boldsymbol{s}_g\} - T_{drift} + \varepsilon \end{aligned} \quad (6)$$

where

$$\begin{aligned} C_l &= C_b^n\left(\boldsymbol{l}_{GNSS}^b\times\right) \\ C_\omega &= \left(\boldsymbol{\omega}_{ie}^n\times\right) + \left(\boldsymbol{\omega}_{en}^n\times\right) \end{aligned} \quad (7)$$

III. RANSAC-Based Fault Detection and Exclusion for GNSS/INS Integration

This section gives a brief introduction to the principle of conventional RANSAC algorithm, and then details in its application and improvement in the tightly coupled GNSS/INS integration.

A. Principle of RANSAC

The RANSAC algorithm utilizes a voting scheme to obtain the optimal model. The implementation of this voting scheme is based on two assumptions: the noisy features will not vote consistently for any single model, and there are sufficient good features. The basic RANSAC algorithm is fundamentally composed of iterative subset sampling and consistency checking [15]. First, a sample subset containing minimal necessary data is randomly selected, and the corresponding model parameters are calculated based on this sample subset. Second, a consistency check is used to distinguish inliers consistent with the model and outliers inconsistent with the model, and the correctness of the model based on the first sample subset is evaluated by the number of inliers. These two steps are iteratively repeated until the model has the highest level of consistency (that is, the highest number of inliers).

For a RANSAC algorithm, there are three main parameters: the sample number of the subset, the inlier judgment threshold and the maximum iteration [15]. The sample number of the subset depends on the minimum number of data elements required for model estimation. The inlier judgment threshold is generally set according to the desired confidence level. RANSAC is a nondeterministic algorithm in the sense that it produces a reasonable result only with a certain probability, with this probability increasing as more iterations are allowed. However, iterating through all subsets is too time-consuming for a large sample, so it is necessary to set an iteration threshold to improve the algorithm efficiency.

B. Subset Selection in TC-GNSS/INS Solution

The number of subset samples is the minimum number of data elements required for model estimation, and it refers to the minimum number of satellites for GNSS positioning in tightly coupled GNSS RTK/INS integration. In the conventional GNSS positioning solution, it is generally believed that at least 4 satellites are required to estimate three-dimensional position and the receiver clock error.

Compared with the conventional GNSS solution, tightly coupled integration increases the INS assistance; therefore, 4 satellites are not necessary. We have previously analyzed the auxiliary effect of different numbers of satellites on the tightly coupled integration, and it will not be repeated in this article. Our preliminary work based on multiple field tests results show that 2 satellites with good geometric distributions can improve the integrated navigation accuracy. Therefore, the number of subset samples is 2 satellites in this article. This is also the advantage of the proposed method over the conventional GNSS solution.

C. Inlier Judgment in TC-GNSS/INS Solution

The inlier judgment is based on whether the observed GNSS range information is consistent with the model formed by the current subset. Here, the integrated navigation results, which are obtained from the tightly coupled integration solution assisted by the 2 satellites in the subset, can be used to perform inverse computation of the range observation. The derived range and the real observed range outside the subset are used to construct the range residual that is the basis of the inlier judgment. The following analysis will illustrate the calculation process of the range residual and its standard deviation with the carrier phase observation as an example.

The between-receiver single-difference carrier phase observation $\tilde{\varphi}_{br}^{s}$ is given in (4); here, it is rewritten as

$$\tilde{\varphi}_{br}^{s} = \frac{1}{\lambda}\rho_{br}^{s} + \frac{1}{\lambda}T_{bias}^{sys} + \Delta N \quad (8)$$

The derived single-difference carrier phase $\hat{\varphi}_{br}^{s}$ can be expressed by

$$\hat{\varphi}_{br}^{s} = \frac{1}{\lambda}\hat{\rho}_{br}^{s} + \frac{1}{\lambda}\hat{T}_{bias}^{sys} + \Delta\hat{N} \quad (9)$$

where $\hat{\rho}_{br}^{s}$ and $\hat{T}_{bias}^{sys}$ can be obtained from the model parameters. However, $\Delta\hat{N}$ is unknown, because the estimated results based on the subset only include the single-difference ambiguity of the selected 2 satellites, and the ambiguity of the remaining satellites outside the subset is presently unknown. Therefore, it is necessary to eliminate the single-difference ambiguity.

In general, the ambiguity remains the same for two adjacent epochs, so it can be removed using the between-epoch difference to yield the following expression.

$$\nabla\Delta\tilde{\varphi}^{s} = \tilde{\varphi}_{br}^{s}\left(t_2\right) - \tilde{\varphi}_{br}^{s}\left(t_1\right) \quad (10)$$

where $\nabla\Delta\tilde{\varphi}^s$ is the double-difference range observation, and the double difference is a between-epoch single difference of a between-receiver single difference; t_1 and t_2 are two adjacent epochs.

According to (9), the derived double-difference carrier phase $\nabla\Delta\hat{\varphi}^s$ can be expressed by

$$\nabla\Delta\hat{\varphi}^s = \frac{1}{\lambda}\left(\hat{\rho}^s_{br}(t_2) + \hat{T}^{sys}_{bias}(t_2)\right) - \frac{1}{\lambda}\left(\hat{\rho}^s_{br}(t_1) + \hat{T}^{sys}_{bias}(t_1)\right) \tag{11}$$

Combining (10) and (11) yields the double-difference carrier phase residual as

$$\delta\varphi^s = \nabla\Delta\hat{\varphi}^s - \nabla\Delta\tilde{\varphi}^s \tag{12}$$

The double-difference carrier phase residual is the basic parameter used for the inlier judgment, and the corresponding variance σ^2 (σ is the corresponding standard deviation) can be written as,

$$\sigma^2 = \sigma_1^2 + \sigma_2^2 \tag{13}$$

where σ_1^2 represents the variance of the derived double-difference carrier phase $\nabla\Delta\hat{\varphi}^s$ and σ_2^2 represents the variance of the observed double-difference carrier phase $\nabla\Delta\tilde{\varphi}^s$.

According to (11), the variance of the derived double-difference carrier phase can be expressed by

$$\sigma_1^2 = \frac{1}{\lambda^2}\left(\sigma_{\rho 2}^2 + \sigma_{t2}^2 + \sigma_{\rho 1}^2 + \sigma_{t1}^2\right) \tag{14}$$

where $\sigma_{\rho 1}^2$ and $\sigma_{\rho 2}^2$ are the variances of the range derived from the INS at the adjacent two epochs; σ_{t1}^2 and σ_{t2}^2 are the variances of the single-difference clock errors at the adjacent two epochs, respectively, and they can be obtained from the state variance matrix of the Kalman filter.

Through linearization expansion and spatial transformation, and ignoring the small effect of the covariance $D_{r\phi}$ between position and attitude, the variance σ_ρ^2 of the range derived from the INS can be written as

$$\sigma_\rho^2 = H_r C_n^e \left(D^n_{r,IMU} + H_\phi D_\phi H_\phi^{\mathrm{T}}\right) {C_n^e}^{\mathrm{T}} H_r^T \tag{15}$$

where H_r is the linearized matrix of the single-difference range; C_n^e is the direction cosine matrix from the navigation frame to the Earth frame; H_ϕ is the designed attitude matrix; $D^n_{r,IMU}$ is the variance matrix of the INS position error; and D_ϕ is the variance matrix of the INS attitude error.

According to (4) and (10), σ_2^2 can be calculated by the following equation.

$$\sigma_2^2 = n_{r2} + n_{b2} + n_{r1} + n_{b1} \tag{16}$$

where n_{r1} and n_{r2} are the variances of the measurement noise of the rover station at the two adjacent epochs; n_{b1} and n_{b2} are the variances of the measurement noise of the base station at the two adjacent epochs.

Theoretically, the constructed double-difference carrier phase residual is normally distributed, so the criterion of the inlier and the outlier can be written as,

$$\begin{cases} \delta\varphi^s < T1, & s \in inlier \\ \delta\varphi^s \geq T1, & s \in outlier \end{cases} \tag{17}$$

where the threshold value (denoted by $T1$ in Section III), which depends on the level of the required confidence, can be set as a multiple of the standard deviation of the residual. For example, the confidence level is 99.73% when the threshold is set to 3σ.

D. Subset Iteration in TC-GNSS/INS Solution

Different from the computer vision, the maximum number of iterations need not be limited when the RANSAC algorithm is applied to fault detection and exclusion of tightly coupled integration. This is because the number of visible satellites is limited, resulting in a small subset size with only 2 satellites. However, subset construction requires consideration of the geometric distribution of these 2 satellites to ensure the accuracy of the tightly coupled integration. From experience, it is better that the azimuth difference between the 2 selected satellites generally ranges from 60º to 120º.

On the basis of the conventional RANSAC algorithm as described in Section III, the proposed algorithm adds the global proportion statistics of faults to ensure detection reliability. The global proportion statistics of faults consist of two steps: recording the number of satellites classified as faults during subset iteration and calculating the percentage of faults for each satellite. Note that when satellites are included in the subset, they are not classified as faults, and there are differences in the number of satellites involved in constructing subsets. To exclude the influence of these factors, the global proportion statistics of the faults can be expressed as

$$R_a = \frac{OC}{SN - ISN} \tag{18}$$

where R_a represents the ratio of faults; OC is the number of satellites classified as faults; SN is the total number of subsets with 2 satellites in the current epoch; and ISN is the number of detected satellites involved in the subset.

The higher the ratio is, the greater the probability that there is a gross error in the satellite observations. Whether the satellite observation is faulty can be determined by comparison with preset the threshold $T3$, and the expression can be written as

$$\begin{cases} R_a < T3, & s \in fault-free \\ R_a \geq T3, & s \in fault \end{cases} \tag{19}$$

In Section IV-B, we will delve into the impact of threshold $T3$ value on fault detection. It's important to note that unlike $T1$, which can be stochastically related to the probability of false positives, $T3$ is determined by balancing the recall and precision of fault detection.

E. Algorithm Framework of RANSAC-Based FDE in TC GNSS/INS Solution

Fig. 2 shows the flow of the RANSAC-based fault detection and exclusion of the tightly coupled integration. Block 1 on the left shows the operations performed for each subset. First, tightly coupled integration based on the 2 selected satellites is conducted to obtain the integrated solution. Second, the double-difference residual and the corresponding standard deviation of

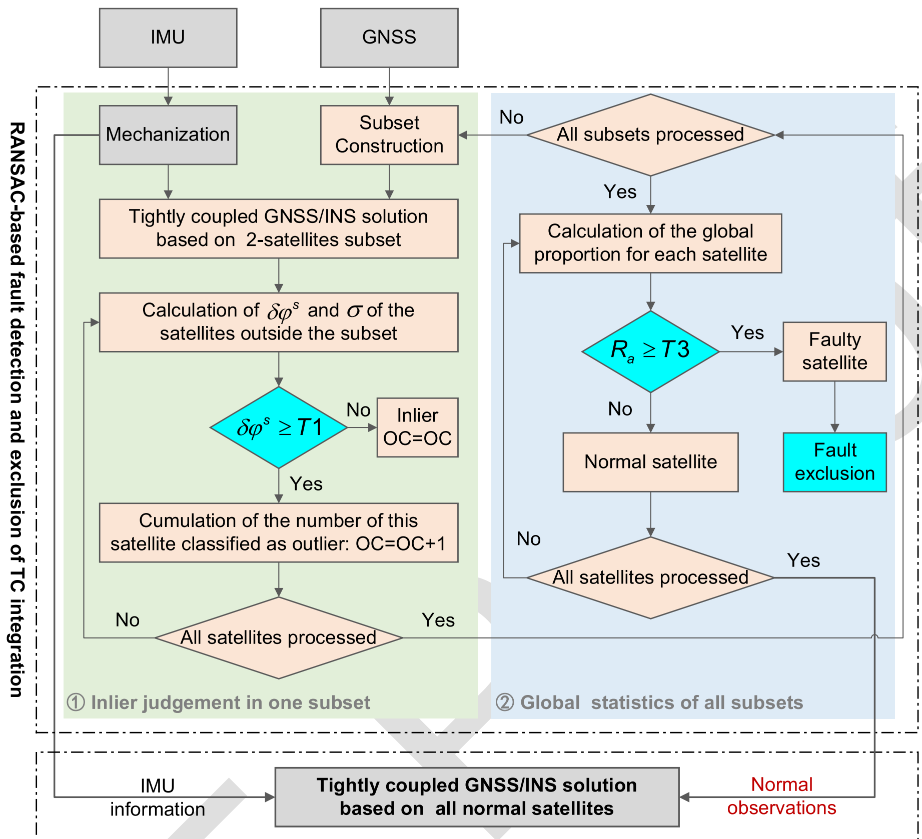

Fig. 2. Flow chart of RANSAC-based fault detection and exclusion of tightly coupled GNSS/INS integration.

satellites outside the subset are calculated. Finally, the residual of each satellite is compared with the preset threshold $T1$, and the number of satellites classified as faults is recorded. Here, threshold $T1$, which is not constant, is related to the standard deviation of the double-difference residual.

The algorithm flow continues to the proposed global fault proportion statistics procedure shown in block ② on the right when all subsets have been iterated and processed. The ratio of satellites classified as faults is calculated and compared with preset threshold $T3$ for reliable fault detection and exclusion. In general, the smaller the threshold is, the easier it is to detect satellite observation faults, but the possibility of false positives is also higher. Conversely, the larger the threshold is, the more difficult it is to detect faults, but the possibility of false positives is also lower. Hence, a reasonable threshold is a key parameter to ensure the effectiveness of fault detection. The effect of the threshold on the detection performance will be analyzed in the following section.

IV. Effect Analysis of Parameters on RANSAC-Based Fault Detection Performance

In this section, we predominantly examine the influence of two parameters on the effectiveness of the proposed RANSAC-based fault detection algorithm: the threshold $T3$ and the quantity of faulty satellites. Our goal is to provide a quantitative analysis of the algorithm's performance. To achieve this, we introduced artificial cycle slips (an example of step errors) with varying magnitudes into the raw carrier phase observations collected from a vehicle-mounted rover receiver in an open-sky environment. The magnitudes are in order as follows: 0.5 cycles, 1.0 cycle, 2.0 cycles and 3.0 cycles, denoted as 0.5c, 1c, 2c, and 3c, respectively. The number of visible satellites was limited to 12. A low-end MEMS grade GNSS/INS system with ICM20602 from TDK InvenSense was used for processing and analysis. Table I lists the optimized specifications of the MEMS IMU.

TABLE I
Optimized Specifications of ICM20602

Sensor	Parameters	ICM20602
Gyro	In-run bias instability (°/hr)	50
	White noise (°/ √ hr)	0.24
Accel.	In-run bias instability (ug)	250
	White noise (m/s/ √ hr)	0.24

A. Performance Evaluation Metrics

For the statistical classification problem, a confusion matrix is a specific table layout that allows visualization of the performance of an algorithm [27]. For binary classification, the scheme of the confusion matrix is shown in Table II. Each row of the matrix represents the instances in an actual class, while each column represents the instances in a predicted class. The

TABLE II
CONFUSION MATRIX FOR BINARY CLASSIFICATION

Total		Predicted class	
		Positive	Negative
Actual class	Positive	True Positive (TP)	False Negative (FN)
	Negative	False Positive (FP)	True Negative (TN)

confusing matrix can make it easy to see whether the system is confusing two classes.

The confusion matrix for binary classification shown in Table II presents four classification results: "TP" is the true positive value, which is the number of positive observations classified correctly; "TN" is the true negative value, which is the number of negative observations classified correctly; "FP" is the false positive value, which is the number of actual negative observations classified as positive; and "FN" is the false negative value, which is the number of actual positive observations classified as negative.

In essence, fault detection is a binary classification problem, so the performance evaluation metrics of the fault detection algorithm were borrowed from the terminology and derivations of a confusion matrix [27]. The calculations of the performance metrics, including the accuracy (ACC), precision (PRE), recall (REC) and F-score (Fs) values, are made according to (20)–(23).

$$ACC = \frac{TP + TN}{TP + TN + FP + FN} \tag{20}$$

$$PRE = \frac{TP}{FP + TP} \tag{21}$$

$$REC = \frac{TP}{FN + TP} \tag{22}$$

$$Fs = 2 \times \frac{PRE \times REC}{PRE + REC} \tag{23}$$

It should be noted that the ACC reflects the probability of observations classified correctly, but it can be misleading if used with imbalanced datasets. The PRE represents the ratio of the detected actual negative observations relative to those classified as negative observations, and the lower the PRE is, the higher the false detection rate. The REC represents the ratio of the detected actual negative observations relative to all actual negative observations, and the lower the REC is, the higher the missed detection rate. The Fs value is the harmonic mean of the PRE and REC.

In fault detection, missed detection can lead to faults being included in the integrated navigation solution and producing incorrect results, while false detection can result in accurate observations not being used to reduce the integrated navigation accuracy. Therefore, while guaranteeing a certain REC level, the PRE magnitude should be considered. In the following, we will utilize these two metrics to analyze the effect of parameters on detection performance, and the analysis results are displayed in the form of a percentage of performance metrics.

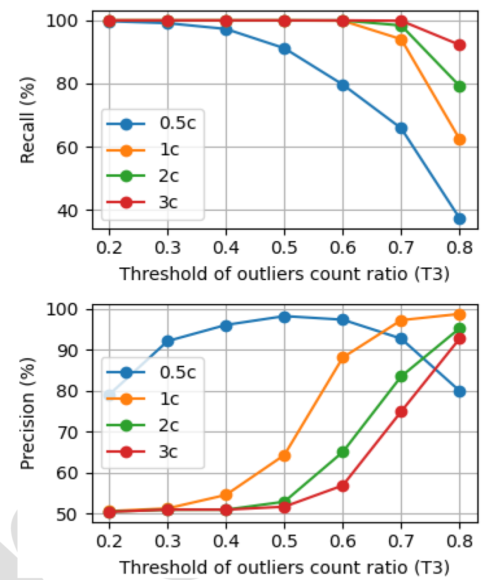

Fig. 3. Performance metric curves representing the effect of threshold $T3$ on RANSAC-based fault detection with different numbers of artificial cycle slips.

B. Effect of Thresholds on Detection Performance

There are two thresholds, $T1$ and $T3$, that need to be set in the proposed fault detection algorithm. The setting of threshold $T1$ will not be discussed in detail, and the judgment is mainly based on the residual sequence of the double-difference carrier phase. Here, the threshold $T1$ is set to 1σ in order to detect small cycle slips (e.g., 0.5-cycle) and effectively capture larger cycle slips (e.g., $>$1-cycle).

Fig. 3 shows the REC and PRE representing the effect of threshold $T3$ on RANSAC-based fault detection with different artificial cycle slips. There are 6 satellites with faults, and threshold $T3$ varies from 0.2 to 0.8. Considering the REC, the value with 0.5 cycle slips is the lowest under the same threshold $T3$, which indicates that the detection of 0.5 cycle slips is the most difficult. The REC values of all cycle slips decrease as threshold $T3$ increases, which indicates that the missed detection rate increases as threshold $T3$ increases.

Considering the PRE, there is less variation in the value with 0.5 cycle slips when threshold $T3$ is changed, and the PRE value can be basically controlled above 80%. The PRE value of 1$\sim$3 cycle slips is less than 60% when threshold $T3$ is less than 0.5 to increase the false detection rate. If a small cycle slip (e.g., less than 0.5c) is the main error, the threshold $T3$ can be set to 0.4. If the large cycle slip (e.g., larger than 1.0c) is the main error, the threshold $T3$ should be set to 0.7. The threshold $T3$ can be set to 0.6 when taking into account cycle slips of 0.5c$\sim$3.0c.

C. Effect of Fault Number on Detection Performance

Fig. 4 shows the performance metric curves representing the effect of the number of faulty satellites on the RANSAC-based fault detection with different artificial cycle slips. The total number of visible satellites is 12, and the number of satellites with artificial faults is 1$\sim$8. The REC value of the detection

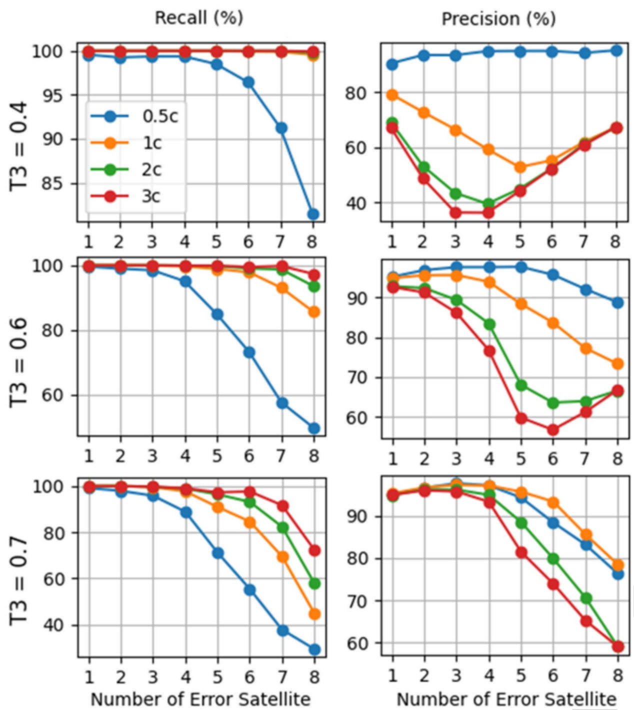

Fig. 4. Performance metrics curves representing the effect of the number of faulty satellites on the RANSAC-based fault detection with different numbers of artificial cycle slips.

Fig. 5. Land vehicle test trajectory segmented with letters (To the left is north, generated by google earth).

TABLE III
SCENARIO DESCRIPTIONS OF DIFFERENT ROAD SEGMENTS

Road segment	Scenario description	Time Proportion
AB	Crossing an urban canyon, GNSS signals were blocked by buildings, and the number of visible satellites was approximately 6.	29.7%
BC	Under a viaduct, the number of visible satellites is less than 6.	15.8%
CD	On a viaduct, and GNSS signals were blocked for 49 seconds at the end of the viaduct due to the noise barrier.	18.2%
DE	Tunnel, there is no GNSS signal.	24.2%
EF	Boulevard, the number of visible satellites is more than 6.	12.1%

algorithm decreases as the number of faulty satellites increases, especially for 0.5 cycle slips. The REC value with 0.5 cycle slips basically remains above 90% when the number of faulty satellites is less than 4.

Different from the REC value, the PRE value does not always decrease as the number of faulty satellites increases. The fluctuation of the PRE curve with 0.5 cycle slips is small, and the overall performance decreases with an increasing number of faulty satellites, while the PRE curves with 1∼3 cycle slips show a trend of first decreasing and then increasing. The larger the threshold $T3$ is, the greater the number of faulty satellites at the minimum value of the curve. The number of faulty satellites corresponding to the minimum value of the curve is 4 and 6 when the threshold $T3$ is 0.4 and 0.6, respectively; the number of faulty satellites is 8 when $T3$ is 0.7, which makes the curve show a monotonically decreasing trend.

For the special trends in the PRE curve, since the total number of satellites is fixed, an increase in the number of faulty satellites results in a decrease in the number of normal satellites. At this time, the detection algorithm has the possibility of false detection, but the number of satellites that can be classified decreases, so the PRE value increases instead.

V. TESTS AND RESULTS

This section presents an analysis of positioning performance in typical urban scenarios and provides statistics from multiple tests conducted in urban environments. Section A focuses on navigation performance in various scenarios, while Section B discusses the effectiveness and availability of the proposed RANSAC-based fault detection and exclusion method.

A. Performance Analysis of Typical Urban Scenarios

To further explore the comprehensive performance of the RANSAC-based fault detection of tightly coupled integration in typical urban scenarios, a land vehicle test covering buildings, tunnels, and viaducts was conducted in Wuhan city. Fig. 5 shows the test trajectory, and the trajectory distance is approximately 4.5 km. The detailed scenario descriptions of different road segments marked with letters are listed in Table III, and the vehicle speed is low in the downtown such as segment AB and BC.

Fig. 6 shows the installation of the equipment used for the field land vehicle test. The INSProbe is a MEMS grade GNSS/INS integrated system with ICM20602 from TDK InvenSense, and a NovAtel OEM718D card is used for GNSS data acquisition. The POS620 is a navigation grade GNSS/INS integrated system with a high-grade fiber optic gyro (FOG), and its postprocessing smoothed results serve as the reference truth for data analysis. The specifications of these two IMUs are listed in Table IV.

Various data processing modes are employed to evaluate the viability of the proposed fault detection method in urban areas. For a detailed description of the data processing mode, see Table V, which outlines the implementation of an innovation-based fault detection method utilizing the tightly coupled GNSS/INS integration.

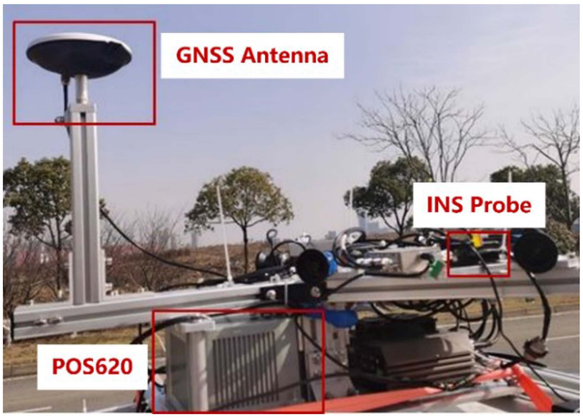

Fig. 6. Installation of the equipment used for the field land vehicle test.

TABLE IV
SPECIFICATIONS OF IMUS

Sensor	Parameters	ICM20602	POS620 (reference)
Gyro	In-run bias instability (°/hr)	50	0.03
	White noise (°/ √ hr)	0.24	0.003
Accel.	In-run bias instability (ug)	250	15
	White noise (m/s/ √ hr)	0.24	0.03

TABLE V
DATA PROCESSING MODE DESCRIPTIONS

	Process Mode	Mode Abbreviation	Description
GNSS RTK		RTK	Forward processing of single frequency GPS/BDS data
GNSS/INS integration	Loosely coupled	LC	Forward filter of RTK/INS loosely coupled integration with robust estimation based on innovation
	Tightly coupled	TC1	Forward filter of RTK/INS tightly coupled integration with robust estimation based on innovation
	Tightly coupled with RANSAC	TC2	Forward filter of RTK/INS tightly coupled integration with RANSAC-based fault detection

Fig. 7 shows the position error of the different processing modes, and the number of satellites, including visible satellites, satellites with cycle slip, and satellites rejected. The GNSS interruption interval is marked on the horizontal axis with a yellow block. Overall, the TC2 mode boasts good position accuracy, particularly in challenging situations, and is supported by the proposed RANSAC-based method for fault detection. The positioning performance is analyzed segment by segment to show the characteristics of different processing modes in different scenarios.

Before segment AB, the RTK mode can maintain a fixed solution. During segment AB, the position accuracy and continuity of the RTK mode are significantly reduced as the number of satellites gradually decreases, and the position accuracy of the LC mode is affected by the GNSS positioning performance.

TABLE VI
PERFORMANCE EVALUATION METRICS DESCRIPTIONS

Metric	Metric Descriptions
Max	Maximum of the absolute value of the navigation error.
RMS	Root mean square of the navigation error.
CDF95	Error value corresponding to the cumulative distribution function with 95%.
Fixed rate	Proportion of epochs with ambiguity correctly fixed.
Valid rate	Proportion of epochs with position error is less than 5.0 m.
Success rate	Proportion of epochs with correct positioning.

For the TC1 and TC2 modes, there is no obvious difference in cycle slip detection and satellite rejection, and the corresponding position accuracy can be controlled within 2.0 m even when there are fewer than 4 satellites. During segment BC, the number of visible satellites is approximately 3$\sim$4, which is caused by severe GNSS signal occlusion caused by the viaduct. Although the position accuracy of all modes is poor, that of the TC1 and TC2 modes can be controlled within 5.0 m and has a relatively good position accuracy compared with the RTK and LC modes.

During segment CD, there is a difference in cycle slip detection and satellite rejection for the TC1 and TC2 modes, and the RANSAC-based fault detection method guarantees the tightly coupled integrated position accuracy of the TC2 mode in the challenging scenario. The correct fault detection of the TC2 mode before entering the tunnel reduces the position error divergence level compared with the TC1 mode. The GNSS signals of segment DE are interrupted for approximately 3 minutes, and the horizontal position error of the TC2 mode diverges to approximately 10 m, while the horizontal position error of the TC1 mode reaches 30 m.

During segment EF, a large number of fault-free satellites were mistakenly eliminated in the TC1 mode, and a long time was required to achieve the convergence of position error. Conversely, the TC2 mode completed the rapid convergence of position error because of the RANSAC-based fault detection method, which effectively controlled the false detection rate and the missed detection rate.

In a typical environment, the RTK and LC modes can experience significant disruption to their positioning performance from external environmental disturbances. However, the TC mode has the capability to leverage the raw GNSS observations to achieve a reliable GNSS/INS integration solution even when the number of satellites is less than four. Notably, the TC2 mode has implemented a RANSAC-based fault detection mechanism to further enhance positioning accuracy in challenging scenarios.

In addition, we also used statistical results for performance evaluation, and the performance evaluation metrics are defined as shown in Table VI.

Fig. 8 shows the performance evaluation metrics of the different processing modes. The position accuracy represented by the Max, RMS and CDF95 of the TC2 mode is significantly better than that of the TC1 and LC modes. Since faults are not correctly detected and eliminated before and after the tunnel, the north position error of the TC1 mode is larger than that of the LC mode. The success rate of the RTK mode is less than 50% because there is frequent GNSS signal interruption

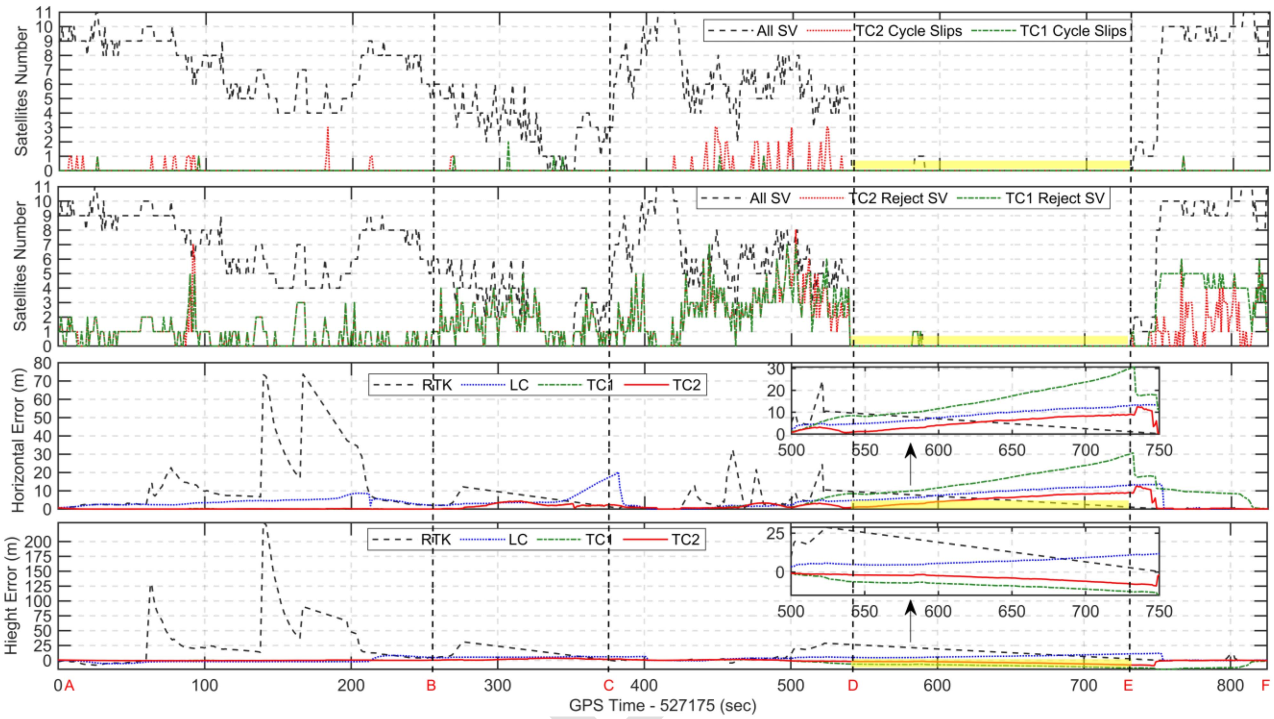

Fig. 7. Position error of the different processing mode and the number of satellites.

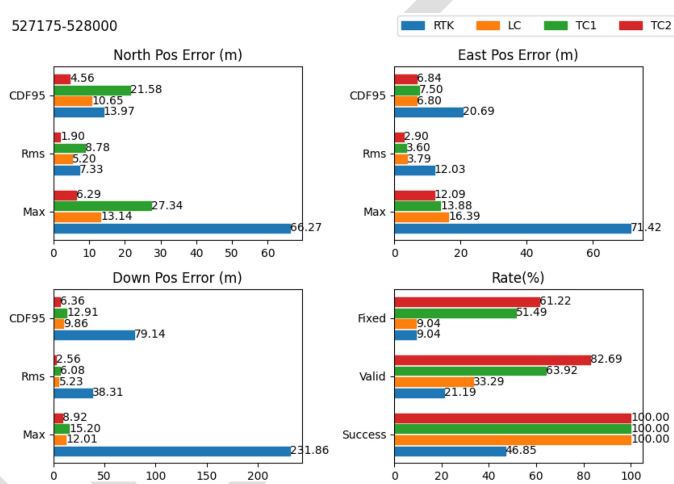

Fig. 8. Performance evaluation metrics of the different processing modes.

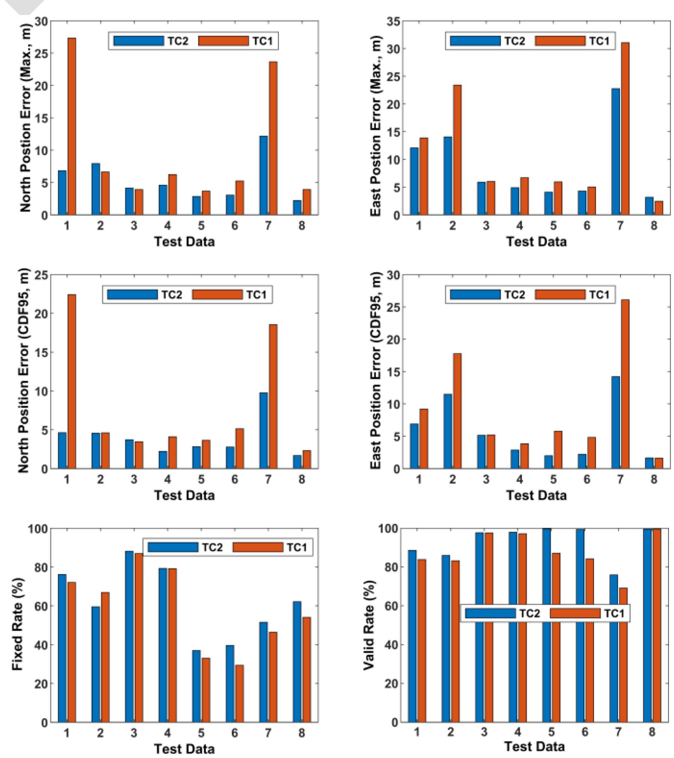

Fig. 9. Performance statistics of multiple tests in urban environment.

caused by the external environment. Although the LC mode can maintain continuous positioning, the corresponding valid rate is only 33%. The valid rate of the two tightly coupled modes is more than 60%, and compared with the TC1 mode, the valid rate and fixed rate of the TC2 mode are increased by 29% and 19%, respectively.

B. Performance Statistics of Multiple Urban Environments

Multiple land vehicle tests were conducted in a complex urban environment to evaluate the feasibility of the RANSAC-based fault detection in tightly coupled integration. Here, the total time length of field test is approximately 7 hours and the environmental conditions include the downtown, campus, city tunnel and viaduct etc. Fig. 9 presents the statistics obtained from these tests. Overall, the maximum position errors and the CDF95 values of the TC2 mode are smaller than those of the

TC1 mode, and the fixed rate and valid rate are significantly higher than those of the TC1 mode. The proposed RANSAC-based fault detection algorithm significantly improved the north and east position accuracy (in terms of CDF95) of the tightly coupled mode in the comprehensive scenario, with an average increase of 45% and 42% respectively. This indicates that the positioning performance of the TC2 mode has been enhanced by the RANSAC-based fault detection algorithm in complex urban environments.

However, in relation to data 2, the TC2 mode displays smaller maximum position errors and CDF95 values compared to the TC1 mode, yet its fixed rate remains lower. This discrepancy suggests that the proposed fault detection algorithm has yielded a high false positive rate, incorrectly classifying normal GNSS observations as faults. The reason behind the unsatisfactory PRE value can be attributed to the greater emphasis given to the REC value for ensuring position error level. This also highlights the flaws in the threshold setting approach of the proposed algorithm. Fixed thresholds may not be suitable for all scenarios, thereby rendering the algorithm inaccurate.

Based on the above analysis of land vehicle tests, it can be seen the TC2 mode can provide navigation information with high performance due to RANSAC-based fault detection and exclusion, and it is better that the thresholds should be adaptively adjusted to ensure the applicability of the proposed algorithm.

VI. Conclusion

This work draws on the application of the RANSAC algorithm for GNSS fault detection, and proposes a RANSAC-based fault detection and exclusion of a tightly coupled GNSS RTK/INS integration for a high-accuracy positioning solution in urban environments. The between-receiver single-difference tightly coupled mode was applied to fully utilize valid GNSS observations. The characteristics of RANSAC-based algorithm for tightly coupled integration were analyzed from the aspects of subset selection, inlier judgment, subset iteration and so on. A fault global proportion statistics was extended to the typical RANSAC algorithm to enhance the detection reliability.

Simulation tests, where artificial cycle slips of different magnitudes were inserted into raw GNSS observations in an open-sky environment, were conducted to analyze the performance of the proposed RANSAC-based fault detection algorithm. The test results show that the proposed algorithm can effectively detect small faults and multiple faults, and the detection rates for 0.5c and 1c$\sim$3c slips were approximately 70% and 90%, respectively. Furthermore, land vehicle tests that included typical scenarios in complex urban environments were conducted to further investigate the comprehensive performance of the proposed algorithm. The results indicate that the tightly coupled mode was more suitable for changeable GNSS environments compared to the loosely coupled mode; and with the help of the proposed RANSAC-based fault detection algorithm, the north and east position accuracy (in terms of CDF95) of the tightly coupled mode in the comprehensive scenario was improved by an average of 45% and 42%.

The proposed RANSAC-based fault detection algorithm can be further applied to multi-sensor information fusion, and guarantee a high level of accuracy and reliability in the positioning solution in harsh urban environments. Our subsequent work will thoroughly compare with the existing methods and optimize the threshold setting scheme to ensure the superiority and universality of the proposed algorithm.

Acknowledgment

The authors thank Yan Wang for the explanation of the RANSAC algorithm in computer vision applications and Jing Fan and Jinwei Shi for the abundant land vehicle test data.

References

[1] N.-E. El Faouzi, H. Leung, and A. Kurian, "Data fusion in intelligent transportation systems: Progress and challenges–A survey," *Inf. Fusion*, vol. 12, no. 1, pp. 4–10, 2011.

[2] H. Jing, Y. Gao, S. Shahbeigi, and M. Dianati, "Integrity monitoring of GNSS/INS based positioning systems for autonomous vehicles: State-of-the-art and open challenges," *IEEE Trans. Intell. Transp. Syst.*, vol. 23, no. 9, pp. 14166–14187, Sep. 2022.

[3] K. Shunsuke, G. Yanlei, and L.-T. Hsu, "GNSS/INS/on-board camera integration for vehicle self-localization in urban canyon," in *Proc. IEEE 18th Int. Conf. Intell. Transp. Syst.*, 2015, pp. 2533–2538.

[4] K. Gunning, J. Blanch, T. Walter, L. D. Groot, and L. Norman, "Integrity for tightly coupled PPP and IMU," in *Proc. 32nd Int. Tech. Meeting Satell. Division Inst. Navigation*, 2019, pp. 3066–3078.

[5] I. Miller, B. Schimpf, M. Campbell, and J. Leyssens, "Tightly-coupled GPS/INS system design for autonomous urban navigation," in *Proc. IEEE/ION Position, Location Navigation Symp.*, 2008, pp. 1297–1310.

[6] G. Blewitt, "An automatic editing algorithm for GPS data," *Geophysical Res. Lett.*, vol. 17, no. 3, pp. 199–202, 1990.

[7] P. J. G. Teunissen, "Quality control in integrated navigation systems," *IEEE Aerosp. Electron. Syst. Mag.*, vol. 5, no. 7, pp. 35–41, Jul. 1990.

[8] R. G. Brown and P. W. McBurney, "Self-contained GPS integrity check using maximum solution separation," *Navigation*, vol. 35, no. 1, pp. 41–53, 1988.

[9] A. El-Mowafy, "GNSS multi-frequency receiver single-satellite measurement validation method," *GPS Solutions*, vol. 18, pp. 553–561, 2014.

[10] J. Blanch, T. Walter, and P. Enge, "Optimal positioning for advanced RAIM," *Navigation: J. Inst. Navigation*, vol. 60, no. 4, pp. 279–289, 2013.

[11] Y. Wen, W. Dai, W. Yu, and L. Pan, "Mitigation of multiple outliers using consistency checking for GNSS standard point positioning in urban areas," *Adv. Space Res.*, Nov. 21, 2023, doi: 10.1016/j.asr.2023.11.023.

[12] T. Strutz, *Data Fitting and Uncertainty: A Practical Introduction to Weighted Least Squares and Beyond*. Berlin, Germany: Springer, 2011.

[13] M. A. Fischler and R. C. Bolles, "Random sample consensus: A paradigm for model fitting with applications to image analysis and automated cartography," *Commun. ACM*, vol. 24, no. 6, pp. 381–395, 1981.

[14] K. G. Derpanis, "Overview of the RANSAC algorithm," *Image Rochester New York*, vol. 4, no. 1, pp. 2–3, 2010.

[15] G. Schroth, A. Ene, J. Blanch, T. Walter, and P. Enge, "Failure detection and exclusion via range consensus," in *Proc. Eur. Navigation Conf.*, 2008, pp. 22–25.

[16] G. Schroth et al., "Enhancements of the range consensus algorithm (RANCO)," in *Proc. 21st Int. Tech. Meeting Satell. Division Inst. Navigation*, 2008, pp. 93–103.

[17] P. D. Groves and Z. Jiang, "Height aiding, C/N0 weighting and consistency checking for GNSS NLOS and multipath mitigation in urban areas," *J. Navigation*, vol. 66, no. 5, pp. 653–669, 2013.

[18] Z. Jiang and P. D. Groves, "GNSS NLOS and multipath error mitigation using advanced multi-constellation consistency checking with height aiding," in *Proc. 25th Int. Tech. Meeting Satell. Division Inst. Navigation*, 2012, pp. 79–88.

[19] X.-L. Su, X. Zhan, J. Tu, and Z. Zhang, "Performance parameters analysis of three levels GNSS integrity monitoring," in *Proc. 28th Int. Tech. Meeting Satell. Division Inst. Navigation*, 2015, pp. 746–763.

[20] G. Castaldo, A. Angrisano, S. Gaglione, and S. Troisi, "P-RANSAC: An integrity monitoring approach for GNSS signal degraded scenario," *Int. J. Navigation Observation*, vol. 2014, 2014, Art. no. 173818.

[21] J. Zhao, C. Xu, Y. Jian, and P. Zhang, "A modified range consensus algorithm based on GA for receiver autonomous integrity monitoring," *Math. Problems Eng.*, vol. 2020, 2020, Art. no. 8969032.

[22] Z. Zhu, E. Vinande, J. Pontious, B. Hall, and N. Shah, "A robust multi-constellation time-differenced carrier phase solution," *GPS Solutions*, vol. 26, no. 1, pp. 1–12, 2022.

[23] D. A. Medina, M. Romanovas, I. Herrera-Pinzón, and R. Ziebold, "Robust position and velocity estimation methods in integrated navigation systems for inland water applications," in *Proc. IEEE/ION Position, Location Navigation Symp.*, 2016, pp. 491–501.

[24] R. Sun, J. Wang, Q. Cheng, Y. Mao, and W. Y. Ochieng, "A new IMU-aided multiple GNSS fault detection and exclusion algorithm for integrated navigation in urban environments," *GPS Solutions*, vol. 25, no. 4, pp. 1–17, 2021.

[25] Q. Zhang, Y. Hu, and X. Niu, "Required lever arm accuracy of non-holonomic constraint for land vehicle navigation," *IEEE Trans. Veh. Technol.*, vol. 69, no. 8, pp. 8305–8316, Aug. 2020.

[26] Y. Gao, Y. Gao, Y. Jiang, and B. Liu, "A modified between-receiver single-difference-based fault detection and exclusion algorithm for real-time kinematic positioning," *IET Radar, Sonar Navigation*, vol. 16, pp. 1269–1281, 2022.

[27] S. V. Stehman, "Selecting and interpreting measures of thematic classification accuracy," *Remote Sens. Environ.*, vol. 62, no. 1, pp. 77–89, 1997.

Quan Zhang (Member, IEEE) received the B.S. degree in geomatics engineering from the Shandong University of Science and Technology, Qingdao, China, in 2009, and the Ph.D. degree from Wuhan University, Wuhan, China, in 2015. From 2017 to 2018, he was a Postdoctoral Researcher with the Digital Photogrammetry Research Group, Lyles School of Civil Engineering, Purdue University, West Lafayette, IN, USA. He is currently an Associate Professor with GNSS Research Center, Wuhan University. His research interests include vehicle-mounted GNSS/INS integration technology and the integrity of multi-sensor integrated navigation for intelligent driving.

Huan Lin received the B.E. degree in geodesy and survey engineering from Wuhan University, Wuhan, China, in 2019. She is currently working toward the master's degree with the GNSS Research Center, Wuhan University. Her research interests include the initial alignment of inertial navigation and robust tightly coupled GNSS/INS integration.

Longyang Ding received the B.E. (Hons.) degree in surveying and mapping engineering from Wuhan University, Wuhan, China, in 2022. He is currently working toward the M.E. degree in navigation, guidance, and control with GNSS Research Center, Wuhan University. His research interests include the GNSS/INS integration for land vehicle navigation and mobile robot state estimation.

Qijin Chen received the B.Eng. and Ph.D. degrees in geodesy and survey engineering from Wuhan University, Wuhan, China, in 2011 and 2016, respectively. He is currently an Associate Research Fellow with GNSS Research Center, Wuhan University. His research interests include the INS with aiding and its applications in geodesy and precise surveying engineering including railway track geometry measuring, and underground pipeline surveying.

Tisheng Zhang received the B.Sc. and Ph.D. degrees in communication and information system from Wuhan University, Wuhan, China, in 2008 and 2013, respectively. From 2018 to 2019, he was a Postdoctoral Researcher with the Hong Kong Polytechnic University, Hong Kong. He is an Associate Professor with the GNSS Research Center, Wuhan University. His research interests include the fields of GNSS receiver and multi-sensor deep integration.

Xiaoji Niu received the B.Eng. degree (Hons.) in mechanical and electrical engineering and the Ph.D. degree from Tsinghua University, Beijing, China, in 1977 and 2002, respectively. From 2003 to 2007, he was a Postdoctoral Fellow with the Mobile Multi-Sensor Systems Research Group, Department of Geomatics Engineering, University of Calgary, Calgary, AB, Canada. From 2007 to 2009, he was a Senior Scientist with SiRF Technology Inc. He is currently a Professor with GNSS Research Center, Wuhan University, Wuhan, China. His research interest focuses on GNSS/INS integration.

RANSAC-Based Fault Detection and Exclusion Algorithm for Single-Difference Tightly Coupled GNSS/INS Integration

Quan Zhang, *Member, IEEE*, Huan Lin, Longyang Ding, Qijin Chen, Tisheng Zhang, and Xiaoji Niu

***Abstract*—There is an urgent need for high-accuracy and high-reliability navigation and positioning in life safety fields such as intelligent transportation and automotive driving, especially in complex urban environments. Although, compared with the GNSS and loosely coupled integration, a tightly coupled GNSS/INS integration can improve the positioning reliability by using raw observations, it still suffers from external challenging environments such as the multipath effect. Therefore, the fault detection algorithm is a premise and guarantee to realize quality control of GNSS/INS integration. Inspired by the application of the random sample consensus (RANSAC) algorithm in GNSS fault detection, this article proposes a RANSAC-based fault detection and exclusion algorithm for single-difference tightly coupled GNSS/INS integration. Here, a between-receiver single-difference (BRSD) model was designed to prevent the consumption of GNSS observations and reduce the waste of effective parameters, and the global proportion statistics of faults were introduced into the typical RANSAC algorithm to further ensure detection reliability. In this study, the effect of the main parameters on the proposed detection algorithm was analyzed and verified by artificial cycle slips. Multiple filed tests, including typical urban scenarios, were conducted to verify the feasibility and effectiveness of the proposed method. The comprehensive test results show that the north and east positioning accuracy in terms of cumulative distribution function (CDF, CDF = 95%) are improved by 45% and 42% over the tightly coupled mode without the proposed detection method.**

***Index Terms*—Fault detection, RANSAC, tightly coupled, between-receiver single difference, GNSS/INS integration.**

Manuscript received 24 October 2023; revised 24 November 2023; accepted 9 December 2023. This work was supported in part by the National Key Research and Development Program of China under Grant 2022YFB3903802, in part by the National Natural Science Foundation of China under Grant 42174024, and in part by AGRS Youth Innovation Foundation under Grant 2020YFL07. *(Quan Zhang and Huan Lin are co-first authors.) (Corresponding authors: Xiaoji Niu; Qijin Chen.)*

Quan Zhang, Qijin Chen, and Tisheng Zhang are with GNSS Research Center, Wuhan University, Wuhan 430072, China, and also with Hubei Luojia Laboratory, Wuhan 430072, China (e-mail: zhangquan@whu.edu.cn; chenqijin@whu.edu.cn; zts@whu.edu.cn).

Huan Lin and Longyang Ding are with GNSS Research Center, Wuhan University, Wuhan 430072, China (e-mail: 2015301610082@whu.edu.cn; dingly@whu.edu.cn).

Xiaoji Niu is with GNSS Research Center, Wuhan University, Wuhan 430072, China, also with Hubei Luojia Laboratory, Wuhan 430072, China, and also with the Artificial Intelligence Institute of Wuhan University, Wuhan 430072, China (e-mail: xjniu@whu.edu.cn).

Color versions of one or more figures in this article are available at https://doi.org/10.1109/TIV.2023.3342274.

Digital Object Identifier 10.1109/TIV.2023.3342274

I. Introduction

The integration of the global navigation satellite system (GNSS) with an inertial navigation system (INS) can achieve complementary advantages, providing pose services with high accuracy and continuity for the intelligent vehicle navigation and control. There has been an increasing demand for the positioning accuracy and reliability of GNSS/INS integration, especially using low-cost sensors (e.g., microelectromechanical system (MEMS) inertial measurement unit (IMU)), in safety of life applications such as intelligent driving [1], [2]. However, complex urban environments bring severe challenges to GNSS observation. For example, satellite visibility is completely or partially obscured in urban environments, which results in a decrease in GNSS positioning accuracy and continuity [3], [4].

Tightly coupled (TC) GNSS/INS integration can directly utilize raw GNSS observations for measurement updates and performs better than loosely coupled (LC) integration in areas with partially blocked GNSS access [5]. Although GNSS/INS integration can ensure positioning continuity, satellite signals are still interfered by the non-line-of-sight (NLOS) signals and multipath effects, resulting in GNSS observation faults and ultimately affecting the positioning accuracy and reliability in challenging environments. Therefore, quality control is a prerequisite to correctly detect faults and improve positioning accuracy and reliability. Common GNSS/INS integration fault detection methods are conducted by constructing test statistics based on the innovation vector of a Kalman filter [6], [7]. These methods apply quality control at the information fusion level and are not effective for multiple faults detection. Classical receiver autonomous integrity monitoring (RAIM) algorithms have been developed to provide fault detection and exclusion (FDE) [8], [9], but they generally work properly in the case of a single fault and cannot provide reliable multiple faults detection capabilities. Although there are some methods such as multiple hypothesis solution separation (MHSS) and an advanced RAIM (ARAIM) method to solving multiple faults, these methods will be ineffective in presence of significantly large biases or large proportion of faulty satellites [10], [11].

Random sample consensus (RANSAC) can achieve correct GNSS fault detection in cases of multiple and small faults, and it is the research hotspot of GNSS fault detection and exclusion [12]. RANSAC is an iterative method to estimate the parameters of a mathematical model from a set of observed data that contains faults, and it can be interpreted as a fault detection method. The RANSAC algorithm was first proposed by Fischler and Bolles [13] and has been widely used in the field of computer vision and is capable of interpreting or smoothing data containing a significant percentage of faults [14]. Schroth et al. [15] first proposed the range consensus (RANCO) algorithm and the suggestion range consensus (S-RANCO) algorithm to detect faulty GNSS range measurements based on the elementary idea of the RANSAC algorithm. Furthermore, Schroth et al. [16] optimized the performance of RANCO by enhancing the subset evaluation, the subset selection algorithm and the modified threshold definition to significantly reduce the missed detection rate and false alarm rate.

On the basis of Schroth's research work, many performance (in terms of accuracy, effectiveness, and stability) improvement methods have been studied. Groves and Jiang et al. [17], [18] applied weighting based on consistency and C/N_0 to the common RANSAC cost function to reduce the number of the largest GNSS faults and used four GNSS measurements plus a height-aiding measurement instead of 5 GNSS measurements to improve the positioning accuracy. Su et al. [19] proposed a fast RANSAC algorithm using geometric dilution of precision (GDOP), the line-of-sight (LOS) vector and singular value decomposition (SVD) for subset preselection to solve the large computational load problem in the traditional RANSAC algorithm. An augmented version of the RANSAC algorithm that performs a final range comparison using the state estimate obtained with only the inliers identified by RANSAC was proposed for more reliable availability [20]. Zhao et al. [21] proposed a modified RANCO algorithm based on a genetic algorithm to inhibit the amount of exponential calculation. In addition, the RANSAC algorithm was introduced to protect the robustness and accuracy of a multi-GNSS time-difference carrier phase (TDCP) solution [22].

Currently, the RANSAC algorithm is applied to the fault detection and exclusion of individual GNSS range measurements, and the relevant research focuses on improving the computational efficiency and fault identification precision. Although some research has utilized the RANSAC algorithm to address the issue of loosely coupled GNSS/INS integration as demonstrated in some studies [23], [24], a critical unresolved problem pertains to the minimum number of satellites required in subset construction. This issue remains unsolved, and it is still necessary to use a minimum of four satellites. The existing relevant research does not design the RANSAC-based algorithm in the tightly coupled GNSS/INS integration, and not fully play the auxiliary role of inertial navigation information in the subset construction.

Inspired by its application to GNSS positioning solutions, RANSAC is applied to single-difference tightly coupled GNSS/INS integration for robust and high-accuracy positioning in this study. The characteristics and contribution of RANSAC-based fault detection in the context of single-difference tightly coupled GNSS/INS integrated navigation can be summarized as follows:

- A between-receiver single-difference (BRSD) tightly coupled GNSS/INS integration mode is designed. This mode reduces the effect of biases such as satellite-related error and atmospheric error, and allows for full utilization of more available GNSS observations.
- Based on the tightly coupled model, a RANSAC-based fault detection algorithm is presented. It can directly utilize two satellites as subset sample with the help of inertial navigation information. In addition, the global proportion statistics method is introduced into the typical RANSAC algorithm to further ensure detection reliability.

This article mainly presents the feasibility of RANSAC-based algorithm to detecting faults in tightly coupled GNSS/INS integration. The rest of this article is organized as follows. Section II illustrates single-difference tightly coupled GNSS/INS integration. Section III briefly introduces the principle of the RANSAC algorithm. Section IV expounds on the RANSAC-based fault detection and exclusion algorithm for single-difference tightly coupled GNSS/INS integration. In Section V, the effect of the main influencing factors on the proposed fault detection method is analyzed and validated. In Section VI, land vehicle tests, including typical scenarios, are conducted, and the experimental results are analyzed and discussed. Finally, the conclusion and characteristics of the proposed RANSAC-based fault detection and exclusion algorithm are summarized in Section VII.

II. Tightly Coupled GNSS/INS Integrated Navigation

An observation model of tightly coupled GNSS/INS integration can be constructed according to a GNSS positioning algorithm. Here, it is based on the between-receiver single-difference model to avoid the consumption of observation information and reduce the waste of effective parameters.

An augmented Kalman filter is applied to online estimate and compensate for sensor errors, including IMU error, single-difference GNSS clock error and ambiguity. Fig. 1 shows a block diagram of tightly coupled GNSS RTK/INS integration. Because tightly coupled GNSS/INS integration research is relatively mature, the design of the state model and observation model is only briefly described.

A. State Model

In GNSS/INS integration, the error state equations of the Kalman filter are commonly based on the error dynamic equations of the INS. The propagation of IMU errors in a given frame can be defined by a set of coupled differential equations based on the inertial navigation equations. Considering the IMU error, the INS error dynamic equations with respect to the navigation reference frame can be written as follows [25]:

$$
\begin{aligned}
\delta\dot{\boldsymbol{r}}^n &= F\cdot\delta\boldsymbol{r}^n + \delta\boldsymbol{v}^n\\
\delta\dot{\boldsymbol{v}}^n &= C_b^n\delta\boldsymbol{f}^b + C_b^n\boldsymbol{f}^b\times\phi - (2\boldsymbol{\omega}_{ie}^n + \boldsymbol{\omega}_{en}^n)\times\delta\boldsymbol{v}^n\\
&\quad + \boldsymbol{v}^n\times(2\delta\boldsymbol{\omega}_{ie}^n + \delta\boldsymbol{\omega}_{en}^n) + \delta\boldsymbol{g}^n\\
\dot{\phi} &= -\boldsymbol{\omega}_{in}^n\times\phi - C_b^n\delta\boldsymbol{\omega}_{ib}^b + \delta\boldsymbol{\omega}_{in}^n\\
\dot{\boldsymbol{b}}_g &= -\frac{1}{T}\boldsymbol{b}_g + \boldsymbol{w}_{bg}\\
\dot{\boldsymbol{b}}_a &= -\frac{1}{T}\boldsymbol{b}_a + \boldsymbol{w}_{ba}
\end{aligned}
$$

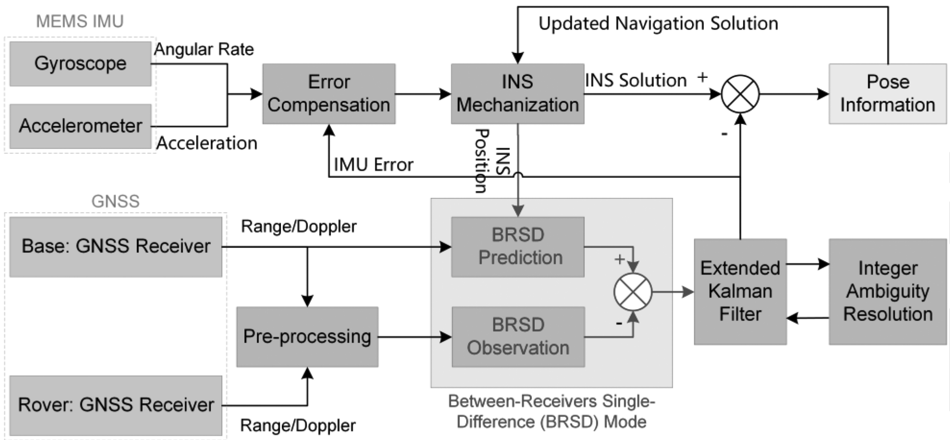

Fig. 1. Block diagram of tightly coupled GNSS RTK/INS integration based on a between-receiver single-difference model.

$$\begin{aligned}\dot{\boldsymbol{s}}_g &= -\frac{1}{T}\boldsymbol{s}_g + \boldsymbol{w}_{sg}\\ \dot{\boldsymbol{s}}_a &= -\frac{1}{T}\boldsymbol{s}_a + \boldsymbol{w}_{sa}\end{aligned} \tag{1}$$

where F is the coefficient matrix of the position error; $\delta\boldsymbol{r}^n$, $\delta\boldsymbol{v}^n$ and ϕ represent the position, velocity and attitude error in the navigation frame, respectively, and $\delta\dot{\boldsymbol{r}}^n$, $\delta\dot{\boldsymbol{v}}^n$ and $\dot{\phi}$ are the corresponding time derivative; $\boldsymbol{f}^b$ is the specific force outputted by the accelerometers; $\delta\boldsymbol{f}^b$ and $\delta\boldsymbol{\omega}_{ib}^b$ represent the sensor errors of the accelerometers and gyroscopes, including the bias ($\boldsymbol{b}_g$ and $\boldsymbol{b}_a$) and scale factor ($\boldsymbol{s}_g$ and $\boldsymbol{s}_a$) which are modeled as 1st Gauss-Markov process (where T is the correlation time and $\boldsymbol{w}$ is the driven white noise) and augmented to the error state vector for online estimation and compensation; C_b^m is the direction cosine matrix from the IMU frame to the navigation frame; $\boldsymbol{\omega}_{en}^n$, $\boldsymbol{\omega}_{ie}^n$ and $\boldsymbol{\omega}_{in}^n$ represent the angular rates of the navigation frame relative to the Earth frame, the Earth frame relative to the inertial frame and the navigation frame relative to the inertial frame in the navigation frame, respectively, and $\delta\boldsymbol{\omega}_{en}^n$, $\delta\boldsymbol{\omega}_{ie}^n$ and $\delta\boldsymbol{\omega}_{in}^n$ are the corresponding angular rate errors; $\delta\boldsymbol{g}^n$ is the normal gravity error at the local position; the superscripts n and b represent the navigation frame and the IMU frame, respectively; and $\times$ represents the cross product of vectors.

A between-receiver single-difference model can reduce the effect of satellite-related errors (e.g., clock error and orbit error) and spatial propagation errors (e.g., ionosphere error and troposphere error) with a baseline up to approximately 10 km [26]. Compared to a double-difference model, a between-receiver single-difference model needs to estimate the receiver clock error. In this article, the GNSS clock model consists of two parameters: clock error a_0 and clock drift a_1, and the drift is modeled as random walk. Hence, the GNSS clock model can be written as

$$\begin{aligned}\dot{a}_0 &= a_1 + w_0\\ \dot{a}_1 &= w_1\end{aligned} \tag{2}$$

where w_0 is the white noise of the clock error and w_1 is the driven white noise of the random walk.

The single-difference ambiguity ΔN is modeled as a random constant, and the corresponding model can be expressed as

$$\Delta\dot{N}_i = 0 \;\; (i = 1, \ldots, m) \tag{3}$$

where m represents the number of single-difference carrier phase observations and i is a visible satellite for the rover and base station in the same epoch.

The tightly coupled GNSS/INS integration state model based on the between-receiver single-difference model can be formed by combining (1), (2) and (3).

B. Observation Model

GNSS observations consist of the pseudorange, carrier phase and Doppler, and the corresponding between-receiver single-difference observation equations can be written as

$$\begin{aligned}\tilde{P}_{br}^s &= P_r^s - P_b^s = \rho_{br}^s + T_{bias}^{sys} + \varepsilon\\ \tilde{\varphi}_{br}^s &= \tilde{\varphi}_r^s - \tilde{\varphi}_b^s = \frac{1}{\lambda}\rho_{br}^s + \frac{1}{\lambda}T_{bias}^{sys} + \Delta N + \varepsilon\\ \tilde{D}_{br}^s &= -\frac{1}{\lambda}\left[\boldsymbol{e}_r^s\left(\boldsymbol{v}^s - \boldsymbol{v}_r\right) - \boldsymbol{e}_b^s\left(\boldsymbol{v}^s - \boldsymbol{v}_b\right)\right] + T_{drift} + \varepsilon\end{aligned} \tag{4}$$

where $\tilde{P}$, $\tilde{\varphi}$ and $\tilde{D}$ are the pseudorange, carrier phase and Doppler observations, respectively; the subscripts r and b represent the rover and base station, respectively; ρ_{br}^s is the single-difference range; T_{bias}^{sys} is the single-difference clock error, and it is the same as a_0 in (2); the superscript s represents a satellite; $T_{drift} = (df_r - df_b)$, and it is the single-difference clock drift that is the same as a_1 in (2); λ is the carrier wavelength; $\boldsymbol{e}_r^s$ and $\boldsymbol{e}_b^s$ are the LOS unit vectors between the rover/base station and the satellite, respectively; $\boldsymbol{v}^s$, $\boldsymbol{v}_r$ and $\boldsymbol{v}_b$ are the velocities of the satellite, rover and base station, respectively; and ε is the observation error.

Here, the expression of the observations derived from inertial navigation is directly given below. The derived range and Doppler observations based on the between-receiver single-difference model can be written as

$$\hat{\rho}_{br}^s = \rho_{br}^s - \boldsymbol{e}_r^s\delta\boldsymbol{r}^n - \boldsymbol{e}_r^s\left[\left(C_b^n\boldsymbol{l}_{GNSS}^b\right)\times\right]\phi$$

$$\hat{D}^s_{br} = -\frac{1}{\lambda}\left[\boldsymbol{e}^s_r\left(\boldsymbol{v}^s-\boldsymbol{v}^n_r\right) - \boldsymbol{e}^s_b\left(\boldsymbol{v}^s-\boldsymbol{v}^n_b\right)\right] + \frac{1}{\lambda}\boldsymbol{e}^s_r\delta\boldsymbol{v}^n \tag{5}$$

where $\boldsymbol{l}^b_{GNSS}$ represents the lever arm between the GNSS antenna and IMU center.

Combining (4) and (5) yields the observation equation of tightly coupled GNSS/INS integration based on the between-receiver single-difference model as follows:

$$\begin{aligned} z_P &= -\boldsymbol{e}^s_r\delta\boldsymbol{r}^n - \boldsymbol{e}^n_r\left[\left(C^n_b\boldsymbol{l}^b_{GNSS}\right)\times\right]\phi - T^{sys}_{bias} + \varepsilon \\ z_\phi &= -\frac{1}{\lambda}\boldsymbol{e}^s_r\delta\boldsymbol{r}^n - \frac{1}{\lambda}\boldsymbol{e}^s_r\left[\left(C^n_b\boldsymbol{l}^b_{GNSS}\right)\times\right]\phi \\ &\quad - \frac{1}{\lambda}T^{sys}_{bias} - \Delta N + \varepsilon \\ z_D &= \frac{1}{\lambda}\boldsymbol{e}^s_r\{\delta\boldsymbol{v}^n - \left[C_\omega\left(C^n_b\boldsymbol{l}^b_{GNSS}\times\right) + \left(C_l\boldsymbol{\omega}^b_{ib}\times\right)\right]\phi - C_l\boldsymbol{b}_g \\ &\quad - C_l diag\left(\boldsymbol{\omega}^b_{ib}\right)\boldsymbol{s}_g\} - T_{drift} + \varepsilon \end{aligned} \tag{6}$$

where

$$\begin{aligned} C_l &= C^n_b\left(\boldsymbol{l}^b_{GNSS}\times\right) \\ C_\omega &= \left(\boldsymbol{\omega}^n_{ie}\times\right) + \left(\boldsymbol{\omega}^n_{en}\times\right) \end{aligned} \tag{7}$$

III. RANSAC-Based Fault Detection and Exclusion for GNSS/INS Integration

This section gives a brief introduction to the principle of conventional RANSAC algorithm, and then details in its application and improvement in the tightly coupled GNSS/INS integration.

A. Principle of RANSAC

The RANSAC algorithm utilizes a voting scheme to obtain the optimal model. The implementation of this voting scheme is based on two assumptions: the noisy features will not vote consistently for any single model, and there are sufficient good features. The basic RANSAC algorithm is fundamentally composed of iterative subset sampling and consistency checking [15]. First, a sample subset containing minimal necessary data is randomly selected, and the corresponding model parameters are calculated based on this sample subset. Second, a consistency check is used to distinguish inliers consistent with the model and outliers inconsistent with the model, and the correctness of the model based on the first sample subset is evaluated by the number of inliers. These two steps are iteratively repeated until the model has the highest level of consistency (that is, the highest number of inliers).

For a RANSAC algorithm, there are three main parameters: the sample number of the subset, the inlier judgment threshold and the maximum iteration [15]. The sample number of the subset depends on the minimum number of data elements required for model estimation. The inlier judgment threshold is generally set according to the desired confidence level. RANSAC is a nondeterministic algorithm in the sense that it produces a reasonable result only with a certain probability, with this probability increasing as more iterations are allowed. However, iterating through all subsets is too time-consuming for a large sample, so it is necessary to set an iteration threshold to improve the algorithm efficiency.

B. Subset Selection in TC-GNSS/INS Solution

The number of subset samples is the minimum number of data elements required for model estimation, and it refers to the minimum number of satellites for GNSS positioning in tightly coupled GNSS RTK/INS integration. In the conventional GNSS positioning solution, it is generally believed that at least 4 satellites are required to estimate three-dimensional position and the receiver clock error.

Compared with the conventional GNSS solution, tightly coupled integration increases the INS assistance; therefore, 4 satellites are not necessary. We have previously analyzed the auxiliary effect of different numbers of satellites on the tightly coupled integration, and it will not be repeated in this article. Our preliminary work based on multiple field tests results show that 2 satellites with good geometric distributions can improve the integrated navigation accuracy. Therefore, the number of subset samples is 2 satellites in this article. This is also the advantage of the proposed method over the conventional GNSS solution.

C. Inlier Judgment in TC-GNSS/INS Solution

The inlier judgment is based on whether the observed GNSS range information is consistent with the model formed by the current subset. Here, the integrated navigation results, which are obtained from the tightly coupled integration solution assisted by the 2 satellites in the subset, can be used to perform inverse computation of the range observation. The derived range and the real observed range outside the subset are used to construct the range residual that is the basis of the inlier judgment. The following analysis will illustrate the calculation process of the range residual and its standard deviation with the carrier phase observation as an example.

The between-receiver single-difference carrier phase observation $\tilde{\varphi}^s_{br}$ is given in (4); here, it is rewritten as

$$\tilde{\varphi}^s_{br} = \frac{1}{\lambda}\rho^s_{br} + \frac{1}{\lambda}T^{sys}_{bias} + \Delta N \tag{8}$$

The derived single-difference carrier phase $\hat{\varphi}^s_{br}$ can be expressed by

$$\hat{\varphi}^s_{br} = \frac{1}{\lambda}\hat{\rho}^s_{br} + \frac{1}{\lambda}\hat{T}^{sys}_{bias} + \Delta\hat{N} \tag{9}$$

where $\hat{\rho}^s_{br}$ and $\hat{T}^{sys}_{bias}$ can be obtained from the model parameters. However, $\Delta\hat{N}$ is unknown, because the estimated results based on the subset only include the single-difference ambiguity of the selected 2 satellites, and the ambiguity of the remaining satellites outside the subset is presently unknown. Therefore, it is necessary to eliminate the single-difference ambiguity.

In general, the ambiguity remains the same for two adjacent epochs, so it can be removed using the between-epoch difference to yield the following expression.

$$\nabla\Delta\tilde{\varphi}^s = \tilde{\varphi}^s_{br}\left(t_2\right) - \tilde{\varphi}^s_{br}\left(t_1\right) \tag{10}$$

where $\nabla\Delta\tilde{\varphi}^s$ is the double-difference range observation, and the double difference is a between-epoch single difference of a between-receiver single difference; t_1 and t_2 are two adjacent epochs.

According to (9), the derived double-difference carrier phase $\nabla\Delta\hat{\varphi}^s$ can be expressed by

$$\nabla\Delta\hat{\varphi}^s = \frac{1}{\lambda}\left(\hat{\rho}^s_{br}(t_2) + \hat{T}^{sys}_{bias}(t_2)\right) - \frac{1}{\lambda}\left(\hat{\rho}^s_{br}(t_1) + \hat{T}^{sys}_{bias}(t_1)\right) \tag{11}$$

Combining (10) and (11) yields the double-difference carrier phase residual as

$$\delta\varphi^s = \nabla\Delta\hat{\varphi}^s - \nabla\Delta\tilde{\varphi}^s \tag{12}$$

The double-difference carrier phase residual is the basic parameter used for the inlier judgment, and the corresponding variance σ^2 (σ is the corresponding standard deviation) can be written as,

$$\sigma^2 = \sigma_1^2 + \sigma_2^2 \tag{13}$$

where σ_1^2 represents the variance of the derived double-difference carrier phase $\nabla\Delta\hat{\varphi}^s$ and σ_2^2 represents the variance of the observed double-difference carrier phase $\nabla\Delta\tilde{\varphi}^s$.

According to (11), the variance of the derived double-difference carrier phase can be expressed by

$$\sigma_1^2 = \frac{1}{\lambda^2}\left(\sigma^2_{\rho 2} + \sigma^2_{t2} + \sigma^2_{\rho 1} + \sigma^2_{t1}\right) \tag{14}$$

where $\sigma^2_{\rho 1}$ and $\sigma^2_{\rho 2}$ are the variances of the range derived from the INS at the adjacent two epochs; σ^2_{t1} and σ^2_{t2} are the variances of the single-difference clock errors at the adjacent two epochs, respectively, and they can be obtained from the state variance matrix of the Kalman filter.

Through linearization expansion and spatial transformation, and ignoring the small effect of the covariance $D_{r\phi}$ between position and attitude, the variance σ_ρ^2 of the range derived from the INS can be written as

$$\sigma_\rho^2 = H_r C_n^e \left(D^n_{r,IMU} + H_\phi D_\phi H_\phi^{\mathrm{T}}\right) C_n^{e\,\mathrm{T}} H_r^T \tag{15}$$

where H_r is the linearized matrix of the single-difference range; C_n^e is the direction cosine matrix from the navigation frame to the Earth frame; H_ϕ is the designed attitude matrix; $D^n_{r,IMU}$ is the variance matrix of the INS position error; and D_ϕ is the variance matrix of the INS attitude error.

According to (4) and (10), σ_2^2 can be calculated by the following equation.

$$\sigma_2^2 = n_{r2} + n_{b2} + n_{r1} + n_{b1} \tag{16}$$

where n_{r1} and n_{r2} are the variances of the measurement noise of the rover station at the two adjacent epochs; n_{b1} and n_{b2} are the variances of the measurement noise of the base station at the two adjacent epochs.

Theoretically, the constructed double-difference carrier phase residual is normally distributed, so the criterion of the inlier and the outlier can be written as,

$$\begin{cases} \delta\varphi^s < T1, & s \in inlier \\ \delta\varphi^s \geq T1, & s \in outlier \end{cases} \tag{17}$$

where the threshold value (denoted by $T1$ in Section III), which depends on the level of the required confidence, can be set as a multiple of the standard deviation of the residual. For example, the confidence level is 99.73% when the threshold is set to 3σ.

D. Subset Iteration in TC-GNSS/INS Solution

Different from the computer vision, the maximum number of iterations need not be limited when the RANSAC algorithm is applied to fault detection and exclusion of tightly coupled integration. This is because the number of visible satellites is limited, resulting in a small subset size with only 2 satellites. However, subset construction requires consideration of the geometric distribution of these 2 satellites to ensure the accuracy of the tightly coupled integration. From experience, it is better that the azimuth difference between the 2 selected satellites generally ranges from 60º to 120º.

On the basis of the conventional RANSAC algorithm as described in Section III, the proposed algorithm adds the global proportion statistics of faults to ensure detection reliability. The global proportion statistics of faults consist of two steps: recording the number of satellites classified as faults during subset iteration and calculating the percentage of faults for each satellite. Note that when satellites are included in the subset, they are not classified as faults, and there are differences in the number of satellites involved in constructing subsets. To exclude the influence of these factors, the global proportion statistics of the faults can be expressed as

$$R_a = \frac{OC}{SN - ISN} \tag{18}$$

where R_a represents the ratio of faults; OC is the number of satellites classified as faults; SN is the total number of subsets with 2 satellites in the current epoch; and ISN is the number of detected satellites involved in the subset.

The higher the ratio is, the greater the probability that there is a gross error in the satellite observations. Whether the satellite observation is faulty can be determined by comparison with preset the threshold $T3$, and the expression can be written as

$$\begin{cases} R_a < T3, & s \in fault-free \\ R_a \geq T3, & s \in fault \end{cases} \tag{19}$$

In Section IV-B, we will delve into the impact of threshold $T3$ value on fault detection. It's important to note that unlike $T1$, which can be stochastically related to the probability of false positives, $T3$ is determined by balancing the recall and precision of fault detection.

E. Algorithm Framework of RANSAC-Based FDE in TC GNSS/INS Solution

Fig. 2 shows the flow of the RANSAC-based fault detection and exclusion of the tightly coupled integration. Block 1 on the left shows the operations performed for each subset. First, tightly coupled integration based on the 2 selected satellites is conducted to obtain the integrated solution. Second, the double-difference residual and the corresponding standard deviation of

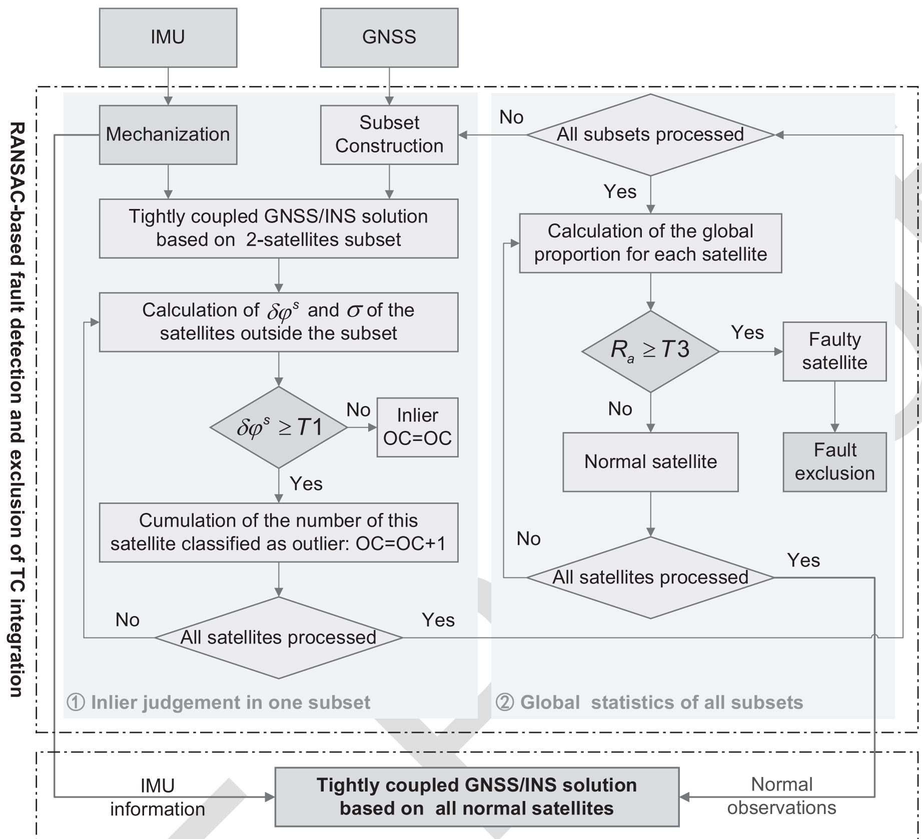

Fig. 2. Flow chart of RANSAC-based fault detection and exclusion of tightly coupled GNSS/INS integration.

satellites outside the subset are calculated. Finally, the residual of each satellite is compared with the preset threshold $T1$, and the number of satellites classified as faults is recorded. Here, threshold $T1$, which is not constant, is related to the standard deviation of the double-difference residual.

The algorithm flow continues to the proposed global fault proportion statistics procedure shown in block ② on the right when all subsets have been iterated and processed. The ratio of satellites classified as faults is calculated and compared with preset threshold $T3$ for reliable fault detection and exclusion. In general, the smaller the threshold is, the easier it is to detect satellite observation faults, but the possibility of false positives is also higher. Conversely, the larger the threshold is, the more difficult it is to detect faults, but the possibility of false positives is also lower. Hence, a reasonable threshold is a key parameter to ensure the effectiveness of fault detection. The effect of the threshold on the detection performance will be analyzed in the following section.

IV. Effect Analysis of Parameters on RANSAC-Based Fault Detection Performance

In this section, we predominantly examine the influence of two parameters on the effectiveness of the proposed RANSAC-based fault detection algorithm: the threshold $T3$ and the quantity of faulty satellites. Our goal is to provide a quantitative analysis of the algorithm's performance. To achieve this, we introduced artificial cycle slips (an example of step errors) with varying magnitudes into the raw carrier phase observations collected from a vehicle-mounted rover receiver in an open-sky environment. The magnitudes are in order as follows: 0.5 cycles, 1.0 cycle, 2.0 cycles and 3.0 cycles, denoted as 0.5c, 1c, 2c, and 3c, respectively. The number of visible satellites was limited to 12. A low-end MEMS grade GNSS/INS system with ICM20602 from TDK InvenSense was used for processing and analysis. Table I lists the optimized specifications of the MEMS IMU.

TABLE I
Optimized Specifications of ICM20602

Sensor	Parameters	ICM20602
Gyro	In-run bias instability (°/hr)	50
	White noise (°/ √ hr)	0.24
Accel.	In-run bias instability (ug)	250
	White noise (m/s/ √ hr)	0.24

A. Performance Evaluation Metrics

For the statistical classification problem, a confusion matrix is a specific table layout that allows visualization of the performance of an algorithm [27]. For binary classification, the scheme of the confusion matrix is shown in Table II. Each row of the matrix represents the instances in an actual class, while each column represents the instances in a predicted class. The

TABLE II
CONFUSION MATRIX FOR BINARY CLASSIFICATION

Total		Predicted class	
		Positive	Negative
Actual class	Positive	True Positive (TP)	False Negative (FN)
	Negative	False Positive (FP)	True Negative (TN)

confusing matrix can make it easy to see whether the system is confusing two classes.

The confusion matrix for binary classification shown in Table II presents four classification results: "TP" is the true positive value, which is the number of positive observations classified correctly; "TN" is the true negative value, which is the number of negative observations classified correctly; "FP" is the false positive value, which is the number of actual negative observations classified as positive; and "FN" is the false negative value, which is the number of actual positive observations classified as negative.

In essence, fault detection is a binary classification problem, so the performance evaluation metrics of the fault detection algorithm were borrowed from the terminology and derivations of a confusion matrix [27]. The calculations of the performance metrics, including the accuracy (ACC), precision (PRE), recall (REC) and F-score (Fs) values, are made according to (20)–(23).

$$ACC = \frac{TP + TN}{TP + TN + FP + FN} \tag{20}$$

$$PRE = \frac{TP}{FP + TP} \tag{21}$$

$$REC = \frac{TP}{FN + TP} \tag{22}$$

$$Fs = 2 \times \frac{PRE \times REC}{PRE + REC} \tag{23}$$

It should be noted that the ACC reflects the probability of observations classified correctly, but it can be misleading if used with imbalanced datasets. The PRE represents the ratio of the detected actual negative observations relative to those classified as negative observations, and the lower the PRE is, the higher the false detection rate. The REC represents the ratio of the detected actual negative observations relative to all actual negative observations, and the lower the REC is, the higher the missed detection rate. The Fs value is the harmonic mean of the PRE and REC.

In fault detection, missed detection can lead to faults being included in the integrated navigation solution and producing incorrect results, while false detection can result in accurate observations not being used to reduce the integrated navigation accuracy. Therefore, while guaranteeing a certain REC level, the PRE magnitude should be considered. In the following, we will utilize these two metrics to analyze the effect of parameters on detection performance, and the analysis results are displayed in the form of a percentage of performance metrics.

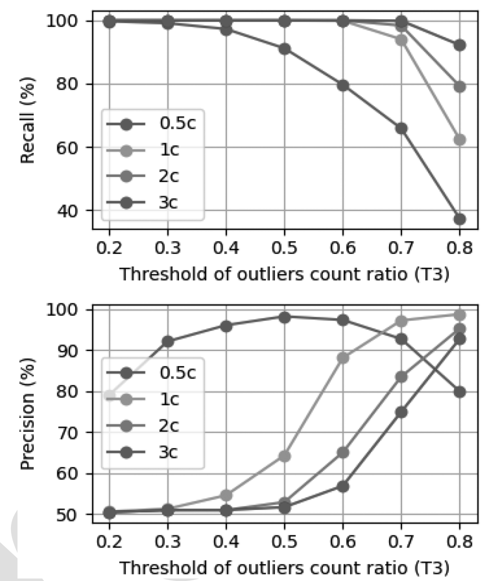

Fig. 3. Performance metric curves representing the effect of threshold $T3$ on RANSAC-based fault detection with different numbers of artificial cycle slips.

B. Effect of Thresholds on Detection Performance

There are two thresholds, $T1$ and $T3$, that need to be set in the proposed fault detection algorithm. The setting of threshold $T1$ will not be discussed in detail, and the judgment is mainly based on the residual sequence of the double-difference carrier phase. Here, the threshold $T1$ is set to 1σ in order to detect small cycle slips (e.g., 0.5-cycle) and effectively capture larger cycle slips (e.g., >1-cycle).

Fig. 3 shows the REC and PRE representing the effect of threshold $T3$ on RANSAC-based fault detection with different artificial cycle slips. There are 6 satellites with faults, and threshold $T3$ varies from 0.2 to 0.8. Considering the REC, the value with 0.5 cycle slips is the lowest under the same threshold $T3$, which indicates that the detection of 0.5 cycle slips is the most difficult. The REC values of all cycle slips decrease as threshold $T3$ increases, which indicates that the missed detection rate increases as threshold $T3$ increases.

Considering the PRE, there is less variation in the value with 0.5 cycle slips when threshold $T3$ is changed, and the PRE value can be basically controlled above 80%. The PRE value of 1$\sim$3 cycle slips is less than 60% when threshold $T3$ is less than 0.5 to increase the false detection rate. If a small cycle slip (e.g., less than 0.5c) is the main error, the threshold $T3$ can be set to 0.4. If the large cycle slip (e.g., larger than 1.0c) is the main error, the threshold $T3$ should be set to 0.7. The threshold $T3$ can be set to 0.6 when taking into account cycle slips of 0.5c$\sim$3.0c.

C. Effect of Fault Number on Detection Performance

Fig. 4 shows the performance metric curves representing the effect of the number of faulty satellites on the RANSAC-based fault detection with different artificial cycle slips. The total number of visible satellites is 12, and the number of satellites with artificial faults is 1$\sim$8. The REC value of the detection

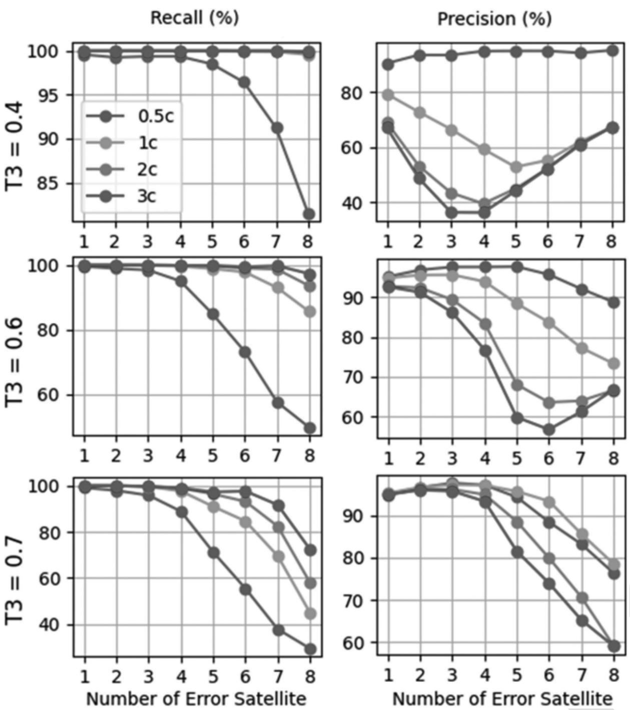

Fig. 4. Performance metrics curves representing the effect of the number of faulty satellites on the RANSAC-based fault detection with different numbers of artificial cycle slips.

Fig. 5. Land vehicle test trajectory segmented with letters (To the left is north, generated by google earth).

TABLE III
SCENARIO DESCRIPTIONS OF DIFFERENT ROAD SEGMENTS

Road segment	Scenario description	Time Proportion
AB	Crossing an urban canyon, GNSS signals were blocked by buildings, and the number of visible satellites was approximately 6.	29.7%
BC	Under a viaduct, the number of visible satellites is less than 6.	15.8%
CD	On a viaduct, and GNSS signals were blocked for 49 seconds at the end of the viaduct due to the noise barrier.	18.2%
DE	Tunnel, there is no GNSS signal.	24.2%
EF	Boulevard, the number of visible satellites is more than 6.	12.1%

algorithm decreases as the number of faulty satellites increases, especially for 0.5 cycle slips. The REC value with 0.5 cycle slips basically remains above 90% when the number of faulty satellites is less than 4.

Different from the REC value, the PRE value does not always decrease as the number of faulty satellites increases. The fluctuation of the PRE curve with 0.5 cycle slips is small, and the overall performance decreases with an increasing number of faulty satellites, while the PRE curves with 1$\sim$3 cycle slips show a trend of first decreasing and then increasing. The larger the threshold $T3$ is, the greater the number of faulty satellites at the minimum value of the curve. The number of faulty satellites corresponding to the minimum value of the curve is 4 and 6 when the threshold $T3$ is 0.4 and 0.6, respectively; the number of faulty satellites is 8 when $T3$ is 0.7, which makes the curve show a monotonically decreasing trend.

For the special trends in the PRE curve, since the total number of satellites is fixed, an increase in the number of faulty satellites results in a decrease in the number of normal satellites. At this time, the detection algorithm has the possibility of false detection, but the number of satellites that can be classified decreases, so the PRE value increases instead.

V. TESTS AND RESULTS

This section presents an analysis of positioning performance in typical urban scenarios and provides statistics from multiple tests conducted in urban environments. Section A focuses on navigation performance in various scenarios, while Section B discusses the effectiveness and availability of the proposed RANSAC-based fault detection and exclusion method.

A. Performance Analysis of Typical Urban Scenarios

To further explore the comprehensive performance of the RANSAC-based fault detection of tightly coupled integration in typical urban scenarios, a land vehicle test covering buildings, tunnels, and viaducts was conducted in Wuhan city. Fig. 5 shows the test trajectory, and the trajectory distance is approximately 4.5 km. The detailed scenario descriptions of different road segments marked with letters are listed in Table III, and the vehicle speed is low in the downtown such as segment AB and BC.

Fig. 6 shows the installation of the equipment used for the field land vehicle test. The INSProbe is a MEMS grade GNSS/INS integrated system with ICM20602 from TDK InvenSense, and a NovAtel OEM718D card is used for GNSS data acquisition. The POS620 is a navigation grade GNSS/INS integrated system with a high-grade fiber optic gyro (FOG), and its postprocessing smoothed results serve as the reference truth for data analysis. The specifications of these two IMUs are listed in Table IV.

Various data processing modes are employed to evaluate the viability of the proposed fault detection method in urban areas. For a detailed description of the data processing mode, see Table V, which outlines the implementation of an innovation-based fault detection method utilizing the tightly coupled GNSS/INS integration.

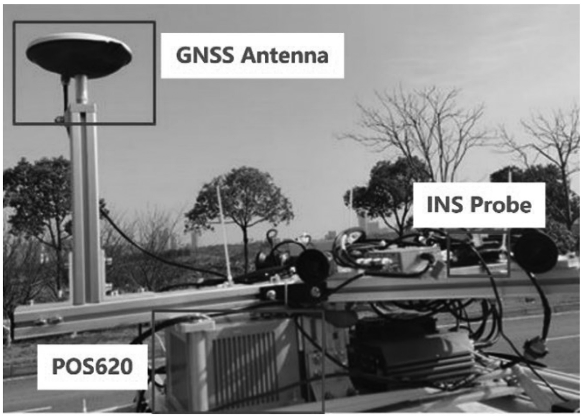

Fig. 6. Installation of the equipment used for the field land vehicle test.

TABLE IV
SPECIFICATIONS OF IMUS

Sensor	Parameters	ICM20602	POS620 (reference)
Gyro	In-run bias instability (°/hr)	50	0.03
	White noise (°/ √ hr)	0.24	0.003
Accel.	In-run bias instability (ug)	250	15
	White noise (m/s/ √ hr)	0.24	0.03

TABLE V
DATA PROCESSING MODE DESCRIPTIONS

Process Mode		Mode Abbreviation	Description
GNSS RTK		RTK	Forward processing of single frequency GPS/BDS data
GNSS/INS integration	Loosely coupled	LC	Forward filter of RTK/INS loosely coupled integration with robust estimation based on innovation
	Tightly coupled	TC1	Forward filter of RTK/INS tightly coupled integration with robust estimation based on innovation
	Tightly coupled with RANSAC	TC2	Forward filter of RTK/INS tightly coupled integration with RANSAC-based fault detection

Fig. 7 shows the position error of the different processing modes, and the number of satellites, including visible satellites, satellites with cycle slip, and satellites rejected. The GNSS interruption interval is marked on the horizontal axis with a yellow block. Overall, the TC2 mode boasts good position accuracy, particularly in challenging situations, and is supported by the proposed RANSAC-based method for fault detection. The positioning performance is analyzed segment by segment to show the characteristics of different processing modes in different scenarios.

Before segment AB, the RTK mode can maintain a fixed solution. During segment AB, the position accuracy and continuity of the RTK mode are significantly reduced as the number of satellites gradually decreases, and the position accuracy of the LC mode is affected by the GNSS positioning performance.

TABLE VI
PERFORMANCE EVALUATION METRICS DESCRIPTIONS

Metric	Metric Descriptions
Max	Maximum of the absolute value of the navigation error.
RMS	Root mean square of the navigation error.
CDF95	Error value corresponding to the cumulative distribution function with 95%.
Fixed rate	Proportion of epochs with ambiguity correctly fixed.
Valid rate	Proportion of epochs with position error is less than 5.0 m.
Success rate	Proportion of epochs with correct positioning.

For the TC1 and TC2 modes, there is no obvious difference in cycle slip detection and satellite rejection, and the corresponding position accuracy can be controlled within 2.0 m even when there are fewer than 4 satellites. During segment BC, the number of visible satellites is approximately 3∼4, which is caused by severe GNSS signal occlusion caused by the viaduct. Although the position accuracy of all modes is poor, that of the TC1 and TC2 modes can be controlled within 5.0 m and has a relatively good position accuracy compared with the RTK and LC modes.

During segment CD, there is a difference in cycle slip detection and satellite rejection for the TC1 and TC2 modes, and the RANSAC-based fault detection method guarantees the tightly coupled integrated position accuracy of the TC2 mode in the challenging scenario. The correct fault detection of the TC2 mode before entering the tunnel reduces the position error divergence level compared with the TC1 mode. The GNSS signals of segment DE are interrupted for approximately 3 minutes, and the horizontal position error of the TC2 mode diverges to approximately 10 m, while the horizontal position error of the TC1 mode reaches 30 m.

During segment EF, a large number of fault-free satellites were mistakenly eliminated in the TC1 mode, and a long time was required to achieve the convergence of position error. Conversely, the TC2 mode completed the rapid convergence of position error because of the RANSAC-based fault detection method, which effectively controlled the false detection rate and the missed detection rate.

In a typical environment, the RTK and LC modes can experience significant disruption to their positioning performance from external environmental disturbances. However, the TC mode has the capability to leverage the raw GNSS observations to achieve a reliable GNSS/INS integration solution even when the number of satellites is less than four. Notably, the TC2 mode has implemented a RANSAC-based fault detection mechanism to further enhance positioning accuracy in challenging scenarios.

In addition, we also used statistical results for performance evaluation, and the performance evaluation metrics are defined as shown in Table VI.

Fig. 8 shows the performance evaluation metrics of the different processing modes. The position accuracy represented by the Max, RMS and CDF95 of the TC2 mode is significantly better than that of the TC1 and LC modes. Since faults are not correctly detected and eliminated before and after the tunnel, the north position error of the TC1 mode is larger than that of the LC mode. The success rate of the RTK mode is less than 50% because there is frequent GNSS signal interruption

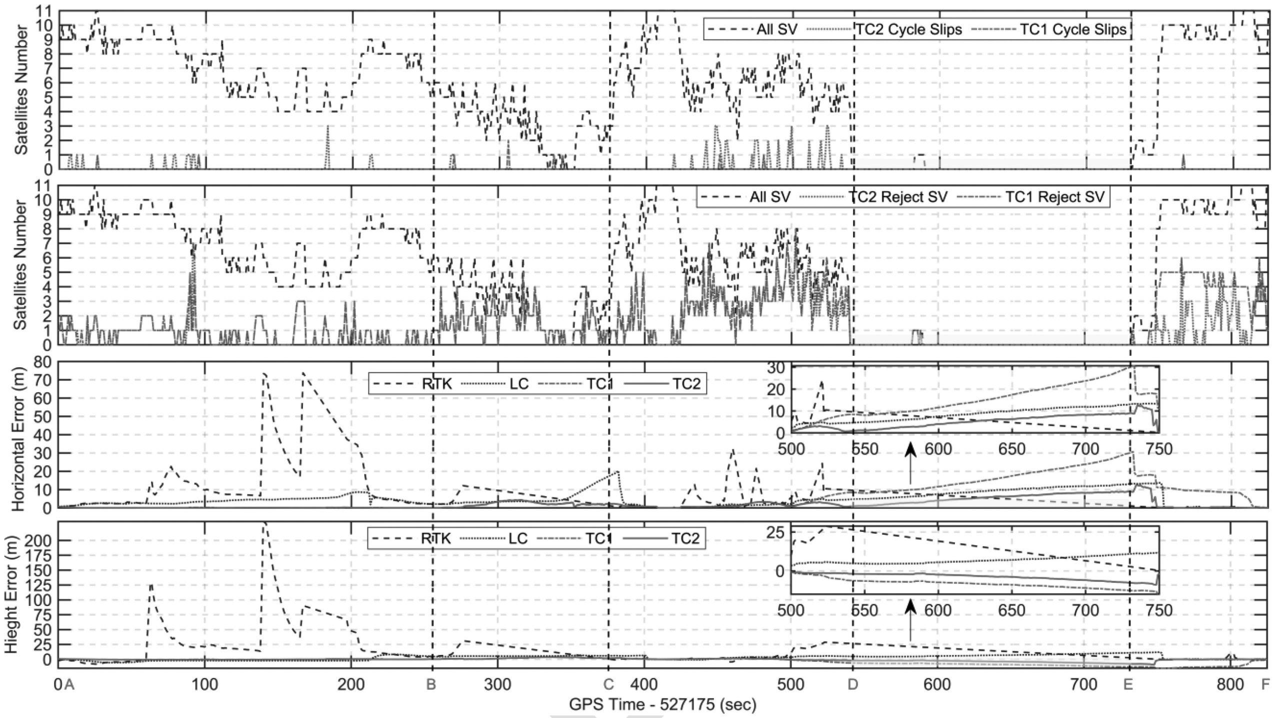

Fig. 7. Position error of the different processing mode and the number of satellites.

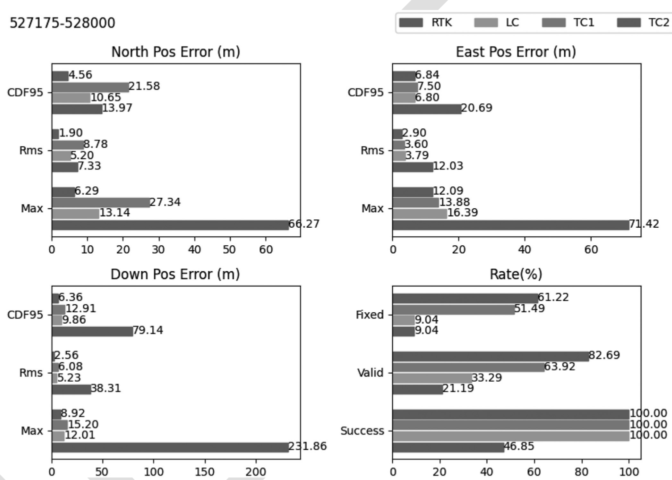

Fig. 8. Performance evaluation metrics of the different processing modes.

caused by the external environment. Although the LC mode can maintain continuous positioning, the corresponding valid rate is only 33%. The valid rate of the two tightly coupled modes is more than 60%, and compared with the TC1 mode, the valid rate and fixed rate of the TC2 mode are increased by 29% and 19%, respectively.

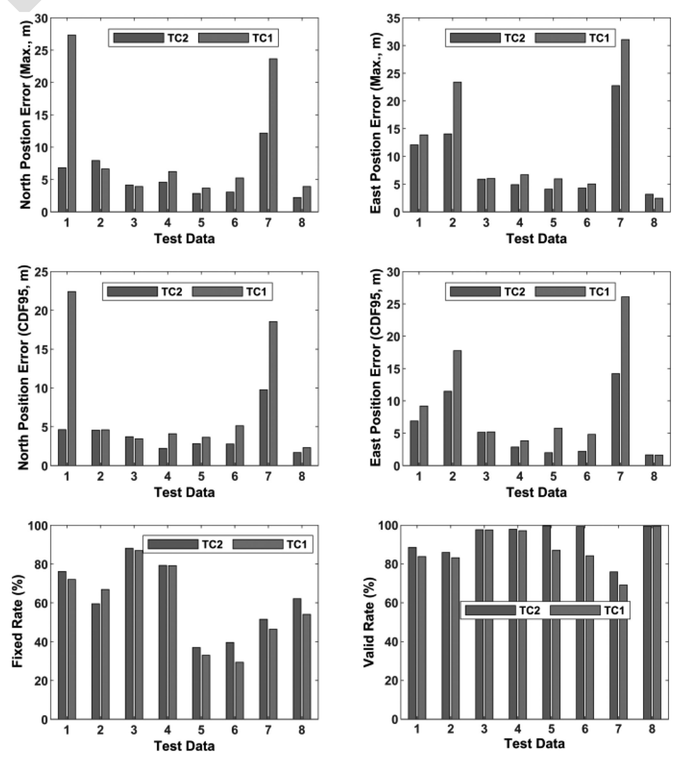

Fig. 9. Performance statistics of multiple tests in urban environment.

B. Performance Statistics of Multiple Urban Environments

Multiple land vehicle tests were conducted in a complex urban environment to evaluate the feasibility of the RANSAC-based fault detection in tightly coupled integration. Here, the total time length of field test is approximately 7 hours and the environmental conditions include the downtown, campus, city tunnel and viaduct etc. Fig. 9 presents the statistics obtained from these tests. Overall, the maximum position errors and the CDF95 values of the TC2 mode are smaller than those of the

TC1 mode, and the fixed rate and valid rate are significantly higher than those of the TC1 mode. The proposed RANSAC-based fault detection algorithm significantly improved the north and east position accuracy (in terms of CDF95) of the tightly coupled mode in the comprehensive scenario, with an average increase of 45% and 42% respectively. This indicates that the positioning performance of the TC2 mode has been enhanced by the RANSAC-based fault detection algorithm in complex urban environments.

However, in relation to data 2, the TC2 mode displays smaller maximum position errors and CDF95 values compared to the TC1 mode, yet its fixed rate remains lower. This discrepancy suggests that the proposed fault detection algorithm has yielded a high false positive rate, incorrectly classifying normal GNSS observations as faults. The reason behind the unsatisfactory PRE value can be attributed to the greater emphasis given to the REC value for ensuring position error level. This also highlights the flaws in the threshold setting approach of the proposed algorithm. Fixed thresholds may not be suitable for all scenarios, thereby rendering the algorithm inaccurate.

Based on the above analysis of land vehicle tests, it can be seen the TC2 mode can provide navigation information with high performance due to RANSAC-based fault detection and exclusion, and it is better that the thresholds should be adaptively adjusted to ensure the applicability of the proposed algorithm.

VI. Conclusion

This work draws on the application of the RANSAC algorithm for GNSS fault detection, and proposes a RANSAC-based fault detection and exclusion of a tightly coupled GNSS RTK/INS integration for a high-accuracy positioning solution in urban environments. The between-receiver single-difference tightly coupled mode was applied to fully utilize valid GNSS observations. The characteristics of RANSAC-based algorithm for tightly coupled integration were analyzed from the aspects of subset selection, inlier judgment, subset iteration and so on. A fault global proportion statistics was extended to the typical RANSAC algorithm to enhance the detection reliability.

Simulation tests, where artificial cycle slips of different magnitudes were inserted into raw GNSS observations in an open-sky environment, were conducted to analyze the performance of the proposed RANSAC-based fault detection algorithm. The test results show that the proposed algorithm can effectively detect small faults and multiple faults, and the detection rates for 0.5c and 1c$\sim$3c slips were approximately 70% and 90%, respectively. Furthermore, land vehicle tests that included typical scenarios in complex urban environments were conducted to further investigate the comprehensive performance of the proposed algorithm. The results indicate that the tightly coupled mode was more suitable for changeable GNSS environments compared to the loosely coupled mode; and with the help of the proposed RANSAC-based fault detection algorithm, the north and east position accuracy (in terms of CDF95) of the tightly coupled mode in the comprehensive scenario was improved by an average of 45% and 42%.

The proposed RANSAC-based fault detection algorithm can be further applied to multi-sensor information fusion, and guarantee a high level of accuracy and reliability in the positioning solution in harsh urban environments. Our subsequent work will thoroughly compare with the existing methods and optimize the threshold setting scheme to ensure the superiority and universality of the proposed algorithm.

Acknowledgment

The authors thank Yan Wang for the explanation of the RANSAC algorithm in computer vision applications and Jing Fan and Jinwei Shi for the abundant land vehicle test data.

References

[1] N.-E. El Faouzi, H. Leung, and A. Kurian, "Data fusion in intelligent transportation systems: Progress and challenges–A survey," *Inf. Fusion*, vol. 12, no. 1, pp. 4–10, 2011.

[2] H. Jing, Y. Gao, S. Shahbeigi, and M. Dianati, "Integrity monitoring of GNSS/INS based positioning systems for autonomous vehicles: State-of-the-art and open challenges," *IEEE Trans. Intell. Transp. Syst.*, vol. 23, no. 9, pp. 14166–14187, Sep. 2022.

[3] K. Shunsuke, G. Yanlei, and L.-T. Hsu, "GNSS/INS/on-board camera integration for vehicle self-localization in urban canyon," in *Proc. IEEE 18th Int. Conf. Intell. Transp. Syst.*, 2015, pp. 2533–2538.

[4] K. Gunning, J. Blanch, T. Walter, L. D. Groot, and L. Norman, "Integrity for tightly coupled PPP and IMU," in *Proc. 32nd Int. Tech. Meeting Satell. Division Inst. Navigation*, 2019, pp. 3066–3078.

[5] I. Miller, B. Schimpf, M. Campbell, and J. Leyssens, "Tightly-coupled GPS/INS system design for autonomous urban navigation," in *Proc. IEEE/ION Position, Location Navigation Symp.*, 2008, pp. 1297–1310.

[6] G. Blewitt, "An automatic editing algorithm for GPS data," *Geophysical Res. Lett.*, vol. 17, no. 3, pp. 199–202, 1990.

[7] P. J. G. Teunissen, "Quality control in integrated navigation systems," *IEEE Aerosp. Electron. Syst. Mag.*, vol. 5, no. 7, pp. 35–41, Jul. 1990.

[8] R. G. Brown and P. W. McBurney, "Self-contained GPS integrity check using maximum solution separation," *Navigation*, vol. 35, no. 1, pp. 41–53, 1988.

[9] A. El-Mowafy, "GNSS multi-frequency receiver single-satellite measurement validation method," *GPS Solutions*, vol. 18, pp. 553–561, 2014.

[10] J. Blanch, T. Walter, and P. Enge, "Optimal positioning for advanced RAIM," *Navigation: J. Inst. Navigation*, vol. 60, no. 4, pp. 279–289, 2013.

[11] Y. Wen, W. Dai, W. Yu, and L. Pan, "Mitigation of multiple outliers using consistency checking for GNSS standard point positioning in urban areas," *Adv. Space Res.*, Nov. 21, 2023, doi: 10.1016/j.asr.2023.11.023.

[12] T. Strutz, *Data Fitting and Uncertainty: A Practical Introduction to Weighted Least Squares and Beyond*. Berlin, Germany: Springer, 2011.

[13] M. A. Fischler and R. C. Bolles, "Random sample consensus: A paradigm for model fitting with applications to image analysis and automated cartography," *Commun. ACM*, vol. 24, no. 6, pp. 381–395, 1981.

[14] K. G. Derpanis, "Overview of the RANSAC algorithm," *Image Rochester New York*, vol. 4, no. 1, pp. 2–3, 2010.

[15] G. Schroth, A. Ene, J. Blanch, T. Walter, and P. Enge, "Failure detection and exclusion via range consensus," in *Proc. Eur. Navigation Conf.*, 2008, pp. 22–25.

[16] G. Schroth et al., "Enhancements of the range consensus algorithm (RANCO)," in *Proc. 21st Int. Tech. Meeting Satell. Division Inst. Navigation*, 2008, pp. 93–103.

[17] P. D. Groves and Z. Jiang, "Height aiding, C/N0 weighting and consistency checking for GNSS NLOS and multipath mitigation in urban areas," *J. Navigation*, vol. 66, no. 5, pp. 653–669, 2013.

[18] Z. Jiang and P. D. Groves, "GNSS NLOS and multipath error mitigation using advanced multi-constellation consistency checking with height aiding," in *Proc. 25th Int. Tech. Meeting Satell. Division Inst. Navigation*, 2012, pp. 79–88.

[19] X.-L. Su, X. Zhan, J. Tu, and Z. Zhang, "Performance parameters analysis of three levels GNSS integrity monitoring," in *Proc. 28th Int. Tech. Meeting Satell. Division Inst. Navigation*, 2015, pp. 746–763.

[20] G. Castaldo, A. Angrisano, S. Gaglione, and S. Troisi, "P-RANSAC: An integrity monitoring approach for GNSS signal degraded scenario," *Int. J. Navigation Observation*, vol. 2014, 2014, Art. no. 173818.

[21] J. Zhao, C. Xu, Y. Jian, and P. Zhang, "A modified range consensus algorithm based on GA for receiver autonomous integrity monitoring," *Math. Problems Eng.*, vol. 2020, 2020, Art. no. 8969032.

[22] Z. Zhu, E. Vinande, J. Pontious, B. Hall, and N. Shah, "A robust multi-constellation time-differenced carrier phase solution," *GPS Solutions*, vol. 26, no. 1, pp. 1–12, 2022.

[23] D. A. Medina, M. Romanovas, I. Herrera-Pinzón, and R. Ziebold, "Robust position and velocity estimation methods in integrated navigation systems for inland water applications," in *Proc. IEEE/ION Position, Location Navigation Symp.*, 2016, pp. 491–501.

[24] R. Sun, J. Wang, Q. Cheng, Y. Mao, and W. Y. Ochieng, "A new IMU-aided multiple GNSS fault detection and exclusion algorithm for integrated navigation in urban environments," *GPS Solutions*, vol. 25, no. 4, pp. 1–17, 2021.

[25] Q. Zhang, Y. Hu, and X. Niu, "Required lever arm accuracy of non-holonomic constraint for land vehicle navigation," *IEEE Trans. Veh. Technol.*, vol. 69, no. 8, pp. 8305–8316, Aug. 2020.

[26] Y. Gao, Y. Gao, Y. Jiang, and B. Liu, "A modified between-receiver single-difference-based fault detection and exclusion algorithm for real-time kinematic positioning," *IET Radar, Sonar Navigation*, vol. 16, pp. 1269–1281, 2022.

[27] S. V. Stehman, "Selecting and interpreting measures of thematic classification accuracy," *Remote Sens. Environ.*, vol. 62, no. 1, pp. 77–89, 1997.

Quan Zhang (Member, IEEE) received the B.S. degree in geomatics engineering from the Shandong University of Science and Technology, Qingdao, China, in 2009, and the Ph.D. degree from Wuhan University, Wuhan, China, in 2015. From 2017 to 2018, he was a Postdoctoral Researcher with the Digital Photogrammetry Research Group, Lyles School of Civil Engineering, Purdue University, West Lafayette, IN, USA. He is currently an Associate Professor with GNSS Research Center, Wuhan University. His research interests include vehicle-mounted GNSS/INS integration technology and the integrity of multi-sensor integrated navigation for intelligent driving.

Huan Lin received the B.E. degree in geodesy and survey engineering from Wuhan University, Wuhan, China, in 2019. She is currently working toward the master's degree with the GNSS Research Center, Wuhan University. Her research interests include the initial alignment of inertial navigation and robust tightly coupled GNSS/INS integration.

Longyang Ding received the B.E. (Hons.) degree in surveying and mapping engineering from Wuhan University, Wuhan, China, in 2022. He is currently working toward the M.E. degree in navigation, guidance, and control with GNSS Research Center, Wuhan University. His research interests include the GNSS/INS integration for land vehicle navigation and mobile robot state estimation.

Qijin Chen received the B.Eng. and Ph.D. degrees in geodesy and survey engineering from Wuhan University, Wuhan, China, in 2011 and 2016, respectively. He is currently an Associate Research Fellow with GNSS Research Center, Wuhan University. His research interests include the INS with aiding and its applications in geodesy and precise surveying engineering including railway track geometry measuring, and underground pipeline surveying.

Tisheng Zhang received the B.Sc. and Ph.D. degrees in communication and information system from Wuhan University, Wuhan, China, in 2008 and 2013, respectively. From 2018 to 2019, he was a Postdoctoral Researcher with the Hong Kong Polytechnic University, Hong Kong. He is an Associate Professor with the GNSS Research Center, Wuhan University. His research interests include the fields of GNSS receiver and multi-sensor deep integration.

Xiaoji Niu received the B.Eng. degree (Hons.) in mechanical and electrical engineering and the Ph.D. degree from Tsinghua University, Beijing, China, in 1977 and 2002, respectively. From 2003 to 2007, he was a Postdoctoral Fellow with the Mobile Multi-Sensor Systems Research Group, Department of Geomatics Engineering, University of Calgary, Calgary, AB, Canada. From 2007 to 2009, he was a Senior Scientist with SiRF Technology Inc. He is currently a Professor with GNSS Research Center, Wuhan University, Wuhan, China. His research interest focuses on GNSS/INS integration.